

An interpretable continuum framework for decision-making: nonreciprocal field theory of the herding control problem

Andrea Lama*

Modeling and Engineering Risk and Complexity, Scuola Superiore Meridionale, Naples, 80125, Italy

Mario di Bernardo†

Department of Electrical Engineering and ICT, University of Naples Federico II, Naples, 80125, Italy

Sabine. H. L. Klapp†

Institute for Theoretical Physics, Technical University Berlin, 10623 Berlin, Germany

(Dated: March 4, 2025)

Field theories for complex systems traditionally focus on collective behaviors emerging from simple, reciprocal pairwise interaction rules. However, many natural and artificial systems exhibit behaviors driven by microscopic decision-making processes that introduce both nonreciprocity and many-body interactions, challenging these conventional approaches. We develop a theoretical framework to incorporate decision-making into field theories using the herding control problem as a paradigmatic example, where agents (herders) must coordinate to confine another group of agents (targets) within a prescribed region. By introducing continuous approximations of two key decision-making elements - target selection and trajectory planning - we derive field equations that capture the essential features of distributed control. Our theory reveals that different decision-making strategies emerge at the continuum level, from random to highly selective choices, and from undirected to goal-oriented motion, driving transitions between homogeneous and confined configurations. The resulting nonreciprocal field theory not only describes the herding problem but provides a general framework for incorporating decision-making into continuum theories of collective behavior, with implications for applications ranging from robotic swarms to crowd management systems.

1. INTRODUCTION

Decision-making is a fundamental process underlying the dynamics of many complex systems in science and technology. At the macroscopic level, the emergent collective behavior of these systems is often shaped by decisions made by individual agents at the microscopic scale. Examples span from animal groups coordinating their movements [1, 2], to autonomous vehicles navigating traffic [3], to robotic swarms performing distributed tasks [4, 5] and decision processes in economics [6]. Often these processes involve a predefined control goal. Understanding how such microscopic decisions translate into macroscopic behavior is crucial for the analysis, design and control of such systems [7]. A versatile, and in many contexts highly efficient, tool to study emergent behaviors on large length and time scales are hydrodynamic continuum equations comprising a set of coupled partial differential equations (PDEs). These not only allow to elucidate the type of instabilities and emerging dynamical states, they can also help to identify relevant mechanisms and parameter ranges in dynamical systems with complex microscopic interaction rules. Yet, the precise translation of microscopic decision rules into continuum descriptions remains a significant challenge in physics and control theory.

Traditional field theories for complex systems often focus on collective behaviors arising from simple, typically reciprocal pairwise interaction rules. Major examples from the physics community are critical phenomena and phase separation in fluid and magnetic systems [8, 9] and, more recently, active [10] and bio-matter [11]. In the last years, much attention has been devoted to *nonreciprocal* generalizations [12, 13] characterized by asymmetrical couplings occurring, e.g., in heterogeneous bacterial systems [14–16], synthetic colloidal mixtures in nonequilibrium environments [17, 18], macroscopic predator-prey systems [19], systems with vision cones [20, 21], but also neural [22] and social [23, 24] networks, and in quantum optics [25–29]. These theories have demonstrated intriguing collective dynamics [12, 13, 30–35], and unusual material properties [36]; however, they do not take into account crucial ingredients of decision-making.

Incorporating decision-making with predefined control objectives introduces distinct challenges: agents must make decisions based on local observations to achieve some desired control goal, a fundamental characteristic of distributed

* andrea.lama-ssm@unina.it

† Correspondence should be addressed to S.K. (sabine.klapp@tu-berlin.de) and M.d.B. (mario.dibernardo@unina.it)

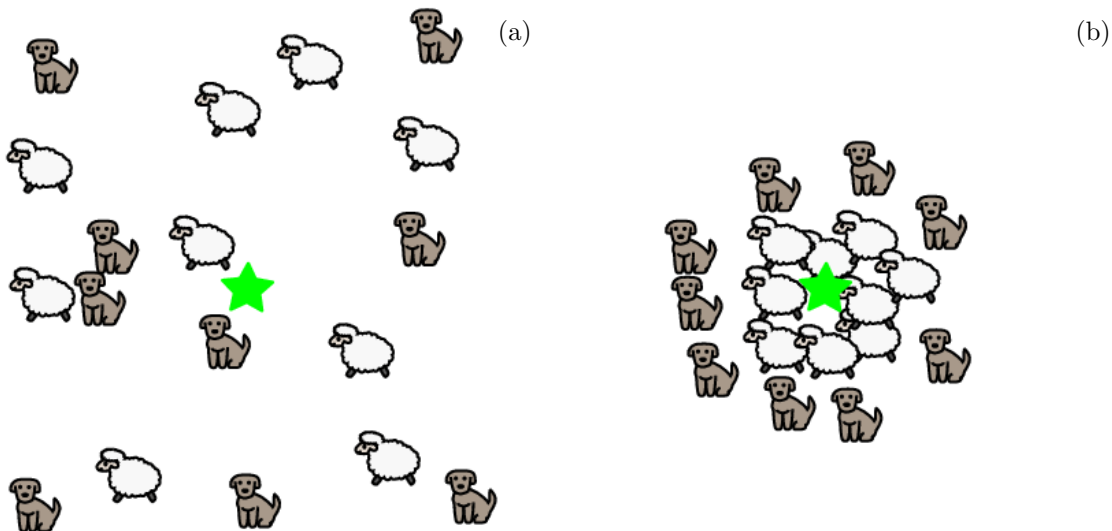


FIG. 1: Illustration of the shepherding task. (a) Initial random configuration of herders (blue) and targets (red), with herders and targets randomly distributed in space and the goal region marked by a green star. (b) Final configuration showing successful containment of targets around the goal region (green star) by the coordinated action of the herders.

feedback control strategies [7]. Here, we demonstrate that the decision-making process induces inherent nonreciprocity and non-pairwise couplings into the system dynamics by explicitly incorporating control objectives, e.g. considering the positions of agents relative to their distance from the goal region. This presents novel challenges for conventional field-theoretic approaches. Here, we propose a framework to address these challenges, using the paradigmatic example of the *shepherding* control problem, where a group of agents, the *herders*, must coordinate themselves to control the collective dynamics of a second group of agents, the *targets*, in a desired way [37].

The shepherding task considered here exemplifies key features of distributed control problems: reliance on local observations and real-time decision-making to achieve global objectives [38, 39]. In our setup, we analyze a representative shepherding task where N_H herders must collect and contain N_T targets within a pre-assigned goal region, which we assume to be a circle centered at the origin (see Fig. 1). To focus on the fundamental aspects of decision-making, we assume that targets exhibit no intrinsic collective properties, such as cohesion, velocity alignment, or coherent response [40], which would otherwise simplify the task [41]. Instead, we model the targets as non-interacting Brownian particles that only experience physical volume exclusion between themselves and are repelled by herders within a distance λ (see Methods).

The key challenge in solving the shepherding control problem lies in the distributed decision-making that determines the dynamics of the herders that must achieve a collective task through local observations. Each herder faces two fundamental decisions that mirror challenges in many real-world control scenarios [7, 42]: which target(s) to influence, and how to influence them. We incorporate these decision-making elements into the dynamics of each herder i through a control input, denoted \mathbf{u}_i (see Methods). This control input takes the form of a feedback term that determines the herder's action based on the relative positions of the observed targets with respect to the goal region.

Following established approaches [37–39], each herder i selects one target with position \mathbf{T}_i^* at each time; specifically, it chooses the target furthest from the origin (i.e., the goal region) within its circular sensing region of radius ξ . To facilitate the derivation of a continuum description that explicitly incorporates decision-making, we employ a continuous approximation of this selection mechanism first proposed in [37].

Specifically, we express \mathbf{T}_i^* as

$$\mathbf{T}_i^* = \frac{\sum_{a \in N_{i,\xi}} e^{\gamma(|\mathbf{T}_a| - |\mathbf{H}_i|)} \mathbf{T}_a}{\sum_{a \in N_{i,\xi}} e^{\gamma(|\mathbf{T}_a| - |\mathbf{H}_i|)}}, \quad (1)$$

where $N_{i,\xi}$ represents the set of targets within herder i 's sensing region, \mathbf{T}_a and \mathbf{H}_i are the two-dimensional (2D) Cartesian coordinates of targets and herders respectively, and $\gamma \geq 0$ is a parameter that controls the selection

specificity. Notice that both the selection rule and the resulting control input, given in Eq. (2) below, incorporate not only pairwise distances between agents, but also each agent’s position relative to the goal. The resulting control has, therefore, a three-body character. The specific expression in Eq. (1), known as a *soft-max* function and widely used in neural networks for output selection [43], enables continuous tuning of the selection rule: as $\gamma \rightarrow \infty$, it recovers the selection of the furthest target, while for $\gamma \rightarrow 0$, \mathbf{T}_i^* approaches the center of mass of all observed targets.

Once a target is selected, the herder positions itself behind it at a distance δ to push it towards the goal. While more sophisticated approaches exist [44, 45], in our minimal shepherding model the dynamics of herder i is subject to an instantaneous feedback control input that can be expressed as:

$$\mathbf{u}_i = - \left(\mathbf{H}_i - (\mathbf{T}_i^* + \delta \widehat{\mathbf{T}}_i^*) \right) \quad (2)$$

where $\widehat{\mathbf{T}}_i^* = \mathbf{T}_i^*/|\mathbf{T}_i^*|$ is the unit vector pointing from the origin to \mathbf{T}_i^* . If no targets are within the sensing radius of herder i , then $\mathbf{u}_i = 0$. This feedback law linearly attracts the herder to the position $\mathbf{T}_i^* + \delta \widehat{\mathbf{T}}_i^*$, enabling it to push the target towards the origin when δ is smaller than the target’s repulsion range λ . Similar to how γ controls target selection, δ provides continuous control over trajectory planning: when $\delta = 0$, the herder approaches \mathbf{T}_i^* from an arbitrary direction, generally failing to push it towards the origin, while for $\delta > 0$, the herder systematically pushes the target towards the origin. Notice that also the trajectory planning, like the selection rule, has a three-body character, depending on the positions of the herder, the selected target, and the goal region.

These two parameters, γ and δ , thus enable us to continuously tune both aspects of decision-making in our system. As demonstrated later in Fig. 3, for sufficiently large γ and appropriate values of δ , the herders successfully confine the targets around the origin, achieving the shepherding task. Conversely, when $\gamma = 0$ and $\delta = 0$, the system evolves to a homogeneous configuration (on average). As detailed in the Methods, our model includes white uncorrelated Gaussian noise for both herders and targets, as well as a reciprocal soft repulsion term between all agents within a distance σ , representing the agents’ diameter, which we assume equal for herders and targets.

A key feature of our system, which will be fundamental in the derivation of the field equations, is its *nonreciprocal* nature. The dynamics violates the action-reaction principle of Newtonian mechanics, which is permissible since this principle only needs to hold at the microscopic level, not at the coarse-grained level of the agents [46]. While nonreciprocal effects have been extensively studied in physics [12, 47], our model reveals a profound connection between nonreciprocity and decision-making: the very act of making decisions introduces fundamental asymmetries into the dynamics. Not only are targets *repelled* by herders while herders are *attracted* to targets, but herders also exhibit decision-making capabilities - selecting targets (γ) and choosing their positions with respect to a goal region (δ) - that have no counterpart in the targets’ dynamics. This intrinsic connection between decision-making and nonreciprocity provides a new perspective on both phenomena, suggesting that nonreciprocal field theories are a natural framework for describing systems with distributed decision-making.

In this work, we show how the continuous approximation of decision-making rules through parameters γ and δ enables the derivation of field equations that capture the macroscopic properties of the shepherding problem. Our analysis reveals that different decision-making strategies, from random to highly selective target choice and from undirected to goal-oriented pushing, emerge in the continuum description. The resulting nonreciprocal field theory is distinctly different from other nonreciprocal scalar theories such as the nonreciprocal Cahn-Hilliard (CH) theory for phase-separation [12, 30] and predator-prey models [19]; it not only successfully describes the shepherding dynamics, including the transition from homogeneous to configurations where targets are confined, but also provides a general framework for incorporating decision-making in presence of a pre-defined control goal into continuum theories of collective behavior. This framework opens new perspectives for analyzing and designing distributed control strategies across diverse applications, from robotic swarm coordination and crowd management to understanding collective animal behavior and developing autonomous transportation systems - scenarios where local decisions fundamentally drive global behavior.

2. RESULTS

A. A field theory for decision-driven shepherding

Our main achievement is a first-principles continuum theory that captures the essential physics of shepherding, derived from microscopic rules of agents’ behavior to predict the emergence of macroscopic patterns. Specifically, we propose a mean field framework for shepherding dynamics based on two coupled partial differential equations (PDEs) that describe the spatio-temporal dynamics of the two species of herders and targets. Each species is represented by scalar, conserved density fields ρ^A , where $A = H$ denotes herders and $A = T$ denotes targets. The dynamics

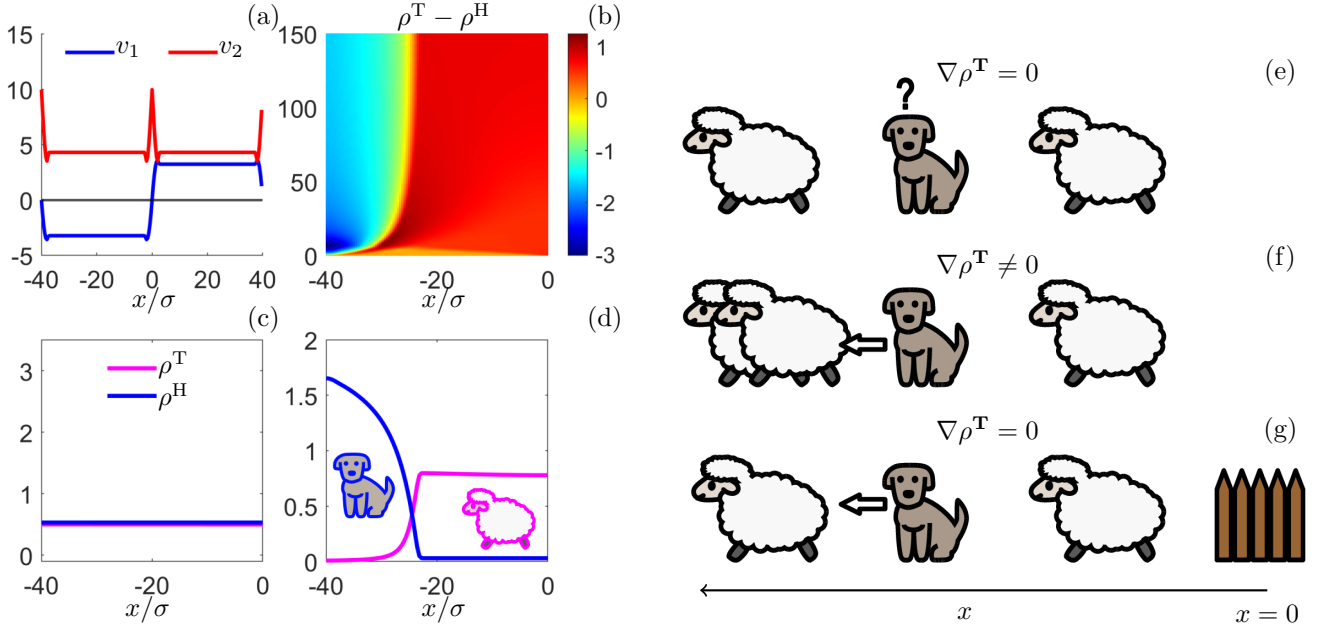


FIG. 2: Field theory description of herding dynamics. (a) The coupling functions v_1 and v_2 generating herding dynamics; v_2 maintains a constant sign reflecting consistent attraction between species, whereas v_1 changes sign depending on the position x of the herders with respect to the goal region $x = 0$, encoding goal-directed behaviour. (b) Spatiotemporal evolution of the density difference $\rho^T - \rho^H$: starting from a homogeneous distribution, the density profiles evolve and saturate to a “shepherding configuration” where ρ^H effectively confines ρ^T in a bounded region around the origin. (c-d) Steady state values of ρ^T and ρ^H for $\gamma = 0$, $\delta = 0$ (c) showing homogeneous distribution and for $\delta > 0$ and $\gamma > 0$ (d) showing confined configuration. (e-g) Representative one-dimensional configurations of targets (sheep) and herders (dog) illustrating the corresponding nonreciprocal couplings in Eq. (4). (e) The herder observes a symmetric distribution of targets ($\nabla\rho^T = 0$), which generates no motion for the herder. (f) The herder observes an asymmetric distribution of targets ($\nabla\rho^T \neq 0$), and moves towards higher targets concentration; this is captured by the coupling the coupling $-v_2\rho^H\nabla\rho^T$. In (g), the target distribution is symmetric again ($\nabla\rho^T = 0$), however the herder also possesses the additional information of the position of the goal region (fence) where to collect the targets. The herder will then move so as to complete the task; this is captured by the coupling term $-v_1(x)\rho^T\rho^H$ in Eq. (4).

incorporate diffusion, conservative interactions, and, most importantly, decision-making elements. For simplicity, we focus on one-dimensional (1D) motion along the x -direction, though generalization to 2D is straightforward. To lowest order, the equations have the form (see Methods)

$$\partial_t \rho^T = \nabla \cdot \left[D^T(\rho^T) \nabla \rho^T + \tilde{k}^T \rho^T \nabla \rho^H \right] \quad (3)$$

$$\partial_t \rho^H = \nabla \cdot \left[D^H(\rho^H) \nabla \rho^H - v_1(x) \rho^H \rho^T - v_2(x) \rho^H \nabla \rho^T \right] \quad (4)$$

The intraspecies coupling in both equations is described by the renormalized diffusivities $D^A(\rho^A)$ which arise from noise and short-range agent-agent repulsion (see Methods). Additionally, the cross-coupling term with coefficient $\tilde{k}^T > 0$ in Eq. (3) combines the effects of both the reciprocal short-range repulsion and the nonreciprocal long-range repulsion exerted by the herders on the targets. This coupling results in the gradient of ρ^H generating a current for ρ^T .

The *decision-making* capability of the herders is captured by the last two terms in Eq. (4) that involve the space-dependent functions $v_1(x; \gamma, \delta)$ and $v_2(x; \gamma, \delta)$. Examples of these functions are plotted in Fig. 2(a), while their analytical expressions are derived in the Methods. The role of the corresponding terms is sketched in Fig. 2 (e-g). The function v_2 , which multiplies the term $\rho^H \nabla \rho^T$, combines two contributions: the short-range reciprocal repulsion between herders and targets and the long-range attraction exerted on a herder by targets at position x . In our parameter regime, v_2 remains strictly positive, causing herders to move preferentially toward regions of higher target concentration (as shown moving leftward in Fig. 2(f)).

In contrast, function v_1 , which multiplies the bilinear term $\rho^H \rho^T$, changes its sign at $x = 0$, the center of the goal region (indicated by a fence in Fig. 2(g)). In particular, v_1 is negative for $x < 0$ and positive for $x > 0$. This change of sign reflects how the direction of chasing depends on the target's location relative to the goal. We may interpret v_1 as a task-dependent speed of herders when a non-zero concentration of targets ρ^T is observed. The consequence is illustrated in Fig. 2(g). Despite observing a symmetric (homogeneous) distribution of targets, the herder preferentially chases the leftmost target due to its greater distance from the fence, representing the goal region. While our agent-based model yields explicit expressions for v_1 and v_2 (see Methods), we expect the overall dynamics to remain robust under small changes of these functions, provided their essential properties – particularly their signs and symmetries – are preserved.

Mathematically, the structure of the decision-making terms in Eq. (4), particularly the coupling term $v_1 \rho^T \rho^H$, emerges from the core properties of our agent-based model. These reflect how herders select which target to pursue (controlled by γ) and how they choose their chasing position (determined by δ). In both decisions, herders consider the positions of the targets relative to their own positions and, most importantly, to the location of the goal region. The equations are derived by expanding the *soft-max* function for \mathbf{T}_i^* in the small γ regime, where $\gamma \lesssim 1/\xi$ (see Methods).

In the absence of decision-making ($\gamma = \delta = 0$), Eq. (3) remains unchanged, while Eq. (4) reduces to

$$\partial_t \rho^H = \nabla \cdot [D^H(\rho^H) \nabla \rho^H - v_2^0 \rho^H \nabla \rho^T] \quad (5)$$

where $v_1(x)|_{\gamma, \delta=0} = 0$, and where $v_2^0 > 0$ and the negative sign in front of the last term reflects the attractive nature of the force acting on a herder by a target (see Methods and Supplementary Information Section II.A for further details on the derivation). Even in this simplest case, the PDE system (3)-(5) is *nonreciprocal* in the sense that the cross-couplings between targets and herders have different signs (or values).

While similar scalar nonreciprocal theories, such as the Cahn-Hilliard models, have been studied extensively [12, 30] in relation to parity-time symmetry breaking and traveling states, our model exhibits a distinctive feature: for nonzero γ and δ , the current experienced by herders emerges from the control-oriented, three-body coupling that depends on the goal region's position. This three-body coupling gives rise to the final terms in Eq. (4). These terms have not only space-dependent "prefactors", they also involve the bilinear nonreciprocal term $v_1(x) \rho^T \rho^H$, which is absent in simpler theories without goal-oriented decision-making. The asymmetry between these terms and those in the simpler target dynamics in Eq.(3) constitutes a fundamental, source of nonreciprocity in the system, which remains unexplored at the field level.

B. Field theory captures agent-based behaviour

Our field equations capture the complex spatial patterns and dynamics observed in agent-based simulations, validating the theoretical framework. To provide a microscopic perspective of the emerging shepherding dynamics, we present simulation snapshots from the underlying agent-based model (see Methods) in Fig. 3. We explore several representative values of the two control parameters: γ , which determines the selectivity, and δ , which controls the trajectory planning, focusing on cases where the number of herders equals the number of targets ($N_H = N_T$) (for other cases, see Supplementary Information Section I.C). The insets of Fig. 3 show the corresponding time-averaged density profiles relative to the origin, $\hat{\rho}^T(r)$ and $\hat{\rho}^H(r)$, where r is the radial distance, obtained by averaging over the polar angle θ .

In the absence of decision-making ($\gamma = \delta = 0$) the system reaches a disordered state [Fig. 3(c)] with homogeneous densities characterized by constant profiles [Fig. 4(c)]. This behaviour is also observed at the continuum level (see Fig. 2(c)). Note that even in this uncontrolled case, the underlying equations of motion remain nonreciprocal. However, for the system parameters considered, this nonreciprocity does not lead to overall symmetry breaking, but only induces microstructural changes (clustering) on the agent-based level, which are not the focus here and will be the subject of future investigation.

The situation changes when one or both of the control parameters γ , δ are nonzero: the system develops inhomogeneities, as illustrated by the density profiles in Figs. 4(a), (b), (d). This behavior reflects a *radial symmetry-breaking* (relative to the case $\gamma = \delta = 0$), where the target density $\hat{\rho}^T(r)$ reaches its maximum at the center and continuously decreases to zero radially outward. The most pronounced effect occurs when γ is large compared to the sensing radius and δ is non-zero, enabling herders to effectively guide their targets toward the desired direction. We then observe a concentrated disk of targets around the center, bounded by a sharp agglomeration of herders [cf. Fig. 4(b)]. When only one control parameter is nonzero, similar but less pronounced inhomogeneities emerge [Figs. 4(a, d)].

A key achievement of our work is that the continuum theory we propose here successfully reproduces the essential features of agent-based density distributions. Two exemplary long-time sets of density profiles (from the numerical

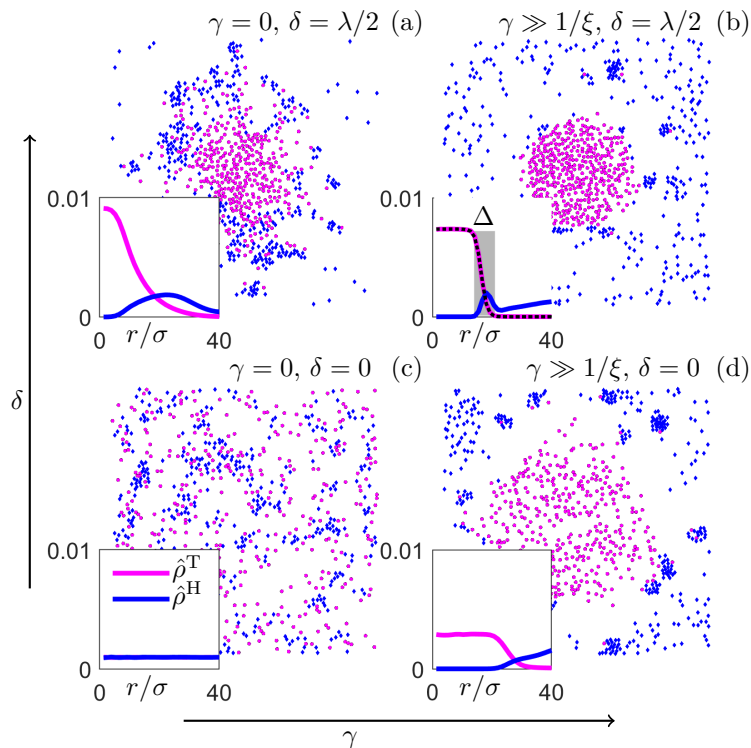


FIG. 3: Long-time configurations and density profiles of the agent-based system under varying control parameters. (a-d) System states for different combinations of selectivity (γ) and trajectory planning (δ) parameters, with insets showing time-averaged and angle-averaged density histograms of targets $\hat{\rho}^T(r)$ and herders $\hat{\rho}^H(r)$ as a function of the radial distance from the origin, r . At $\gamma = \delta = 0$ we observe a disordered state with (on average) homogeneous density distribution (c). The other panels show that, as soon as δ or γ are non zero, inhomogeneous configurations are reached, where herders tend to surround targets. The inset of panel (b) shows the fit of the target profile to a hyperbolic tangent (black dashed line) and indicates with a shaded grey rectangle the target-herder interface of width Δ , see Methods for further details.

solution of (3) and (4) are shown in Figs. 2(c-d), revealing a striking similarity with their agent-based counterparts, despite differences in geometry (1D versus 2D) and specific values of γ and δ . Agent-based simulations in Supplementary Information Section I.D, where we consider a rectangular rather than circular goal region, further substantiate our claim that 1D field theories can capture the emergence of containment of the 2D agent-based dynamics.

Indeed, in the absence of decision-making [Fig. 2(c)], the field theory produces a stable homogeneous state (note that temporal instabilities are absent at the parameters considered, see Supplementary Information Section II.B). With decision-making, the spatiotemporal evolution of the density difference $\rho^T(x, t) - \rho^H(x, t)$ in Fig. 2(b) clearly demonstrates the emergence of inhomogeneities and finally the saturation into a steady state with density profiles shown in Fig. 2(d). In this state, the targets are concentrated within the goal region around $x = 0$, confined by herders accumulating at larger distances, creating a sharp interface between these two spatial domains. This configuration matches the expected outcome of successful shepherding, see Fig. 1.

Importantly, the appearance of the inhomogeneous steady state is a direct consequence of the nonreciprocal coupling arising from decision-making in our field equations. A stable homogeneous steady state solution exists only in the absence of decision-making (i.e., $\gamma = \delta = 0$, $v_1 = 0$) (see Supplementary Information Section II.B). This solution ceases to be a steady state solution for *any* nonzero value of γ , δ . Indeed, evaluated at the homogeneous solutions $\rho^A = \rho_0^A(t)$, the herder equation (4) reads

$$\partial_t \rho_0^H(t) = -\frac{d}{dx} v_1(x; \gamma, \delta) \rho_0^T \rho_0^H. \quad (6)$$

Thus, when v_1 becomes space-dependent (which occurs for nonzero γ , δ), no homogeneous steady state exists. This holds at any order in the gradient expansion of the densities (see Supplementary Information Section II.A).

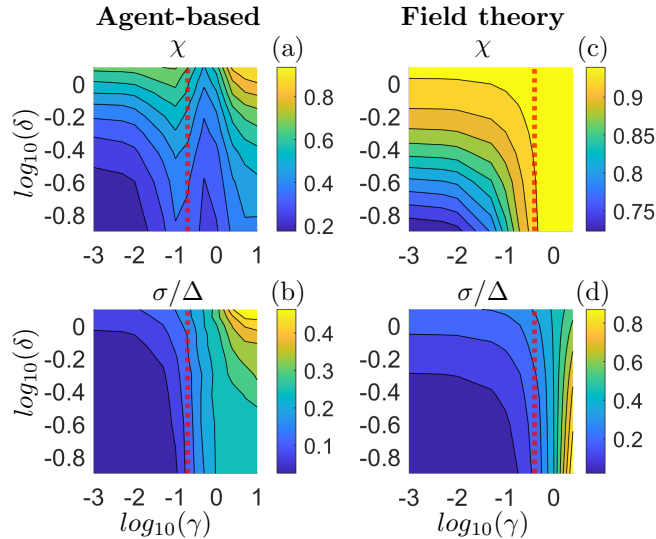


FIG. 4: Comparison of the values of χ (fraction of contained targets) and σ/Δ (sharpness of the herder-target interface) in the (γ, δ) plane for (a-b) the agent-based model and (c-d) the field theory. For small values of γ , where the linearization made to derive the field equations is justified, the level curves show that the results of the agent-based model and of the field theories are consistent. Some differences appear around $\gamma \sim \sigma/\xi$ (red dashed line) where the non-linearity of the selection rule (1) becomes non negligible, hence where the linear approximation performed to derive the field equations starts to fail. A notable difference is that the combined maximum value of the two order parameters is reached for large γ and δ for the agent-based model, and for large γ and small δ on a field level.

C. Phase Diagrams of Shepherding States

Our analysis clearly reveals the emergence of inhomogeneous steady states whose details depend on two decision-making parameters. To quantify similarities and differences within these steady states, we analyze two key measures. First, we calculate the fraction χ of targets confined within a circle of radius R around the origin, a metric commonly used to evaluate shepherding performance [37, 45]. Here, R corresponds to the position of the interface shown in Fig. 3(b) (Fig. 2(d) for the continuum case). Second, we evaluate the width of the interfacial region, Δ , where the density $\hat{\rho}^T$ transitions from a non-zero value near the origin to zero at large distances. For details on the definition and calculation of R and Δ in both agent-based and continuum descriptions, see Methods.

Results for both the levels of description for χ and the inverse width (“sharpness”) σ/Δ as functions of the control parameters γ and δ are shown in Fig. 4. Starting from the agent-based results [Figs. 4 (a-b)], we see that both quantities approach their minimum value in the limits $\gamma \rightarrow 0$, $\delta \rightarrow 0$, as expected. The roles of γ and δ are comparable for relatively small values, particularly when $\gamma \lesssim 1/\xi$ (red dashed line). Only beyond this value the nonlinearity of the selection rule in expression (1) becomes relevant. The level-sets of χ , represented by $\delta(\gamma)$, show non-monotonic behavior in γ around this value. The largest values of χ and σ/Δ occur when both γ and δ are large, confirming their roles as order parameters for the shepherding state [37].

For comparison, continuum results for χ and σ/Δ are shown in Figs. 4 (c-d). As in the agent-based case, χ and σ/Δ reach their minimum values at $\gamma \rightarrow 0$, $\delta \rightarrow 0$. As γ and δ increase from small values, χ increases monotonically with both parameters. This differs from the agent-based case [Fig. 4(a)], where the level sets of χ , $\delta(\gamma)$, exhibit non-monotonic behavior around $\gamma = 1/\xi$. This difference arises because the continuum equations employ a linearization with respect to γ (see Methods), valid for $\gamma \lesssim 1/\xi$, a constraint absent in the agent-based case.

Notably, the sharpness reaches its maximum values at *small* δ , a counterintuitive result explained by the competing roles of v_1 and v_2 at the continuum level (see Supplementary Information Section II.C). Despite these differences in detailed dependencies, the field theoretical results confirm that the decision-making parameters γ and δ fundamentally shape the characteristics of the shepherding state. This demonstrates the theory’s ability to describe complex, self-organizing behaviors driven by control-oriented, nonreciprocal interactions.

D. Design Principles for Decision-driven Collective behavior in Natural and Artificial Systems

Our field theory framework reveals fundamental design principles for the emergence of decision-driven collective behaviour in multi-agent systems that extend beyond the basic containment task that we focused on so far. Through appropriate choice of the functions v_1 and v_2 in Eq. (4), we can generate a variety of controlled collective states that could serve as building blocks to capture behaviour observed in both natural and artificial engineered systems. These principles emerge more clearly when we examine how different choices of these coupling functions lead to distinct collective behaviours at long times, as illustrated in Fig. 5.

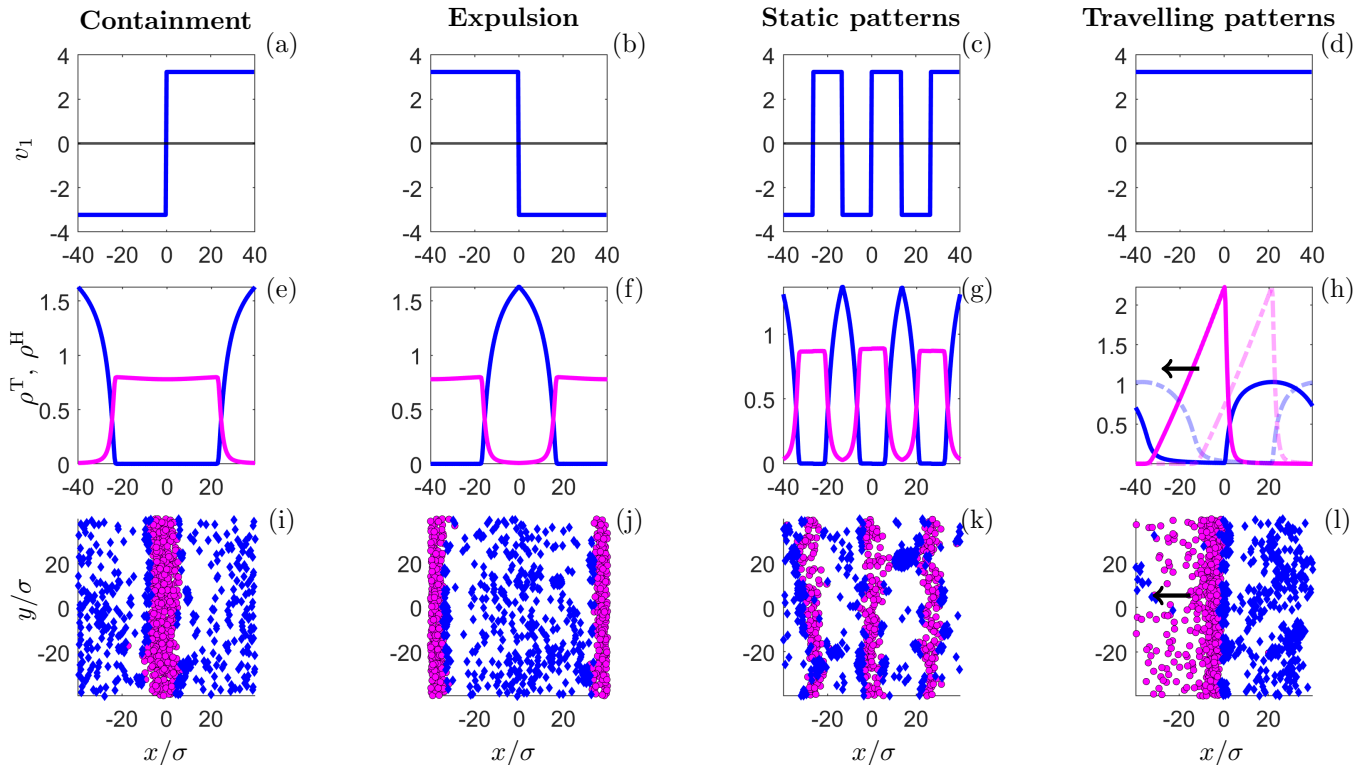


FIG. 5: Diverse collective state on the field level and at the agent-based level upon varying the control input and, thereby, the decision-making rules. (a-d) Possible choices of the function $v_1(x)$, which we set as a square wave with different periods (a-c) or a constant (d). (e-h) the corresponding steady state behaviours of the field equations. (i-l) The corresponding steady state behaviours of the agent-based model; see Supplementary Information Section III.B for details on the agent-based and field equations. By suitable choosing $v_1(x)$, starting from a homogeneous state, we can achieve (i,e) *confinement* of the targets, as discussed above, (f,j) *expulsion* of the targets, e.g. the herders expel the targets out from a region around the origin, (g,k) *static patterns*, and (h,l) *traveling patterns* (see Supplementary Information Video 3 and 4.); in (h) we also plot in shaded dashed lines the densities at a previous time to show that the pattern is moving coherently in time.

The function $v_1(x)$, which multiplies the product of density fields $\rho^T \rho^H$ in Eq. (4), plays a particularly crucial role as it encodes the task-dependent speed of herders. For simplicity, we set $v_1(x)$ to a square wave with different periods or phase shifts, while $v_2(x)$ is set to a positive constant (that, in this setting, represents an effective attraction of herders by targets). By choosing different spatial profiles for $v_1(x)$, we can generate (see Supplementary Videos):

- *Containment*: When $v_1(x)$ changes sign from positive to negative at $x = 0$, the targets remain confined to the goal area centered around the origin [Fig. 5(e)];
- *Expulsion*: Reversing the sign pattern, targets are expelled from a predefined region [Fig. 5(f)];
- *Static patterns*: When $v_1(x)$ alternates between positive and negative values periodically in space, stable, stationary stripe-like arrangements of targets are induced, [Fig. 5(g)];
- *Traveling patterns*: When $v_1(x)$ is set to a constant, non-zero value throughout space $v_1(x) = \tilde{v}_1$, targets and herders create traveling waves that propagate through the system [Fig. 5(h)].

These examples indicate that already simple manipulations of the control coupling functions that encode basic rules for how agents make decisions, can induce a range of behaviors. For example, changes of sign of $v_1(x)$ and the location of the corresponding zeros can be used to realize desired static patterns without changing other coupling parameters. Such patterns are of interest, e.g., in swarm robotics [48] and in engineered bacterial populations [49, 50]. Moreover, already the simplest choice for $v_1(x)$, namely a constant value, generates a traveling pattern (see Supplementary Information Section III.C for further details). We note that stripe-like and travelling patterns also emerge from other PDEs well established in the physics literature, such as reaction-diffusion systems [51] and variants of the nonreciprocal Cahn-Hilliard model studied recently [12, 30].

The key insight presented here is that, in decision-making systems, such diverse behaviors can emerge solely from varying decision-making rules of the herders. For example, we can generate travelling patterns in a parameter regime where such patterns are absent without decision-making (see Supplementary Information Section III.C). This perspective is further substantiated by agent-based simulation results (in the case of a rectangular goal region) shown in the bottom panel of Fig. 5. To generate these results we did not change the microscopic interactions between the two types of agents, but only adapted the decision-making rules of the herders (see Supplementary Information Section III.B), using the same two-step strategy as in the shepherding problem: a proper selection rule, and a proper trajectory planning that finally determines $v_1(x)$ (see Supplementary Information Section III.A further details). The fact that we can create such different collective behaviors by only modifying $v_1(x)$ suggests a unifying principle that may be common to both natural and engineered systems. Most notably, these behaviors emerge naturally from our field equations without requiring changes to their fundamental structure, indicating that our framework captures essential features of decision-driven collective behavior that extend beyond the specific task we considered.

3. DISCUSSION

Our analysis uncovers a fundamental connection between microscopic decision-making and collective behavior: agents' decision-making capabilities inherently generate both nonreciprocity and entirely new forms of coupling in their continuum description. This led us to discover a novel class of nonreciprocal interactions that has remained unexplored in the physics literature [12, 30].

The coupling we derive, which originates from feedback control at the microscopic level (2) and involves a predefined goal, manifests as shepherding behavior at the continuum scale [Fig. 2(b)]. This breakthrough establishes a rigorous mathematical framework connecting individual decision-making to collective behavior, unifying concepts from physics and control theory. In the field of shepherding, that we have chosen as a paradigmatic example, our continuum framework can be systematically extended and refined: For example, it would be very easy to incorporate other types of microscopic interactions such as, e.g., cohesion or alignment, that would lead to additional couplings of the form $\nabla \cdot [\rho^A \nabla \rho^B]$ familiar from Cahn-Hilliard-like theories. Further, applications in higher dimensions could reveal additional instabilities. Indeed, given recent experiments in human coordination [38], we expect a polar instability induced by oscillatory motion of herders around targets. Another conceptually interesting question concerns changes imposed by considering nonlinear terms in the expansion of the selection rule.

The mathematical framework we developed here, where agents select whom to influence and how based on some control goal, can have implications beyond the specific shepherding task considered. Similar decision-making processes might play a role in biological systems, from marine predators [52] and killer whales [53] containing fish schools for hunting, to terrestrial cases like chimpanzee packs defending territories [54] and ant colonies coordinating excavation [55]. Similar principles might be present in social systems as well, particularly in opinion dynamics, [56] where influencers shape followers' opinion consensus by targeting certain individuals [57], and extend to human coordination [38, 58], or engineered systems like swarm robotics [37, 59], where artificial agents can be designed according to this paradigm. However, experimental validation would be needed to determine whether these natural systems actually employ similar mechanisms, an interesting open problem left for future study.

From a more conceptual perspective, our framework addresses an open challenge at the frontier between control theory and complex systems: steering collective behavior in large-scale multi-agent systems to solve distributed control tasks. While advances have been made in controlling complex networks [7], distributed control of mobile agents faces unique challenges. Recent approaches in the field of active matter span optimal control [60, 61], interaction design [20], feedback mechanisms [62], and machine learning [63, 64]. Technically, at the agent level, two fundamental obstacles persist: the scaling of the number of dynamical equations with agent numbers and the time-varying nature of interaction matrices [65, 66]. These challenges are particularly acute in shepherding, where the control of the targets is achieved indirectly through herder dynamics [67].

Here, we propose to tackle these challenges in complex, multi-agent systems by deriving a continuum macroscopic description where the functions $v_1(x)$ and $v_2(x)$ emerge as natural *control inputs* for shaping collective behavior. This aligns with growing interest from both physics [68] and control-theory communities to derive suitable partial differential

equations that capture collective dynamics while incorporating precise control goals [69]. The resulting PDEs provide insights that hold across different system sizes and are insensitive to specific microscopic initial conditions - which are often impossible to prescribe in real-world applications anyway.

In the present work we have provided some first examples of how deliberate manipulation of the control input v_1 and v_2 leads to a variety of collective behaviors. Future research could focus on application of machine learning techniques to actually *learn* the functions v_1 and v_2 directly from experimental data of natural or artificial systems exhibiting decision-driven collective behavior. Similar strategies have been recently used to predict suitable PDEs for active and biological matter [70]. A related intriguing question is to which extent such learned functions could provide new insight into microscopic decision rules and interactions. The framework could also be extended to incorporate more sophisticated decision-making mechanisms, such as those including memory effects or adaptive learning. Furthermore, investigating the interplay between noise, decision-making, and collective dynamics could reveal novel dynamical phases and transition mechanisms. Ultimately, such PDEs should predict not only steady-state behavior but also spatiotemporal patterns and even hierarchical self-organisation as it was recently found in biological communicating systems [71]. The connection between nonreciprocity and decision-making uncovered here also suggests new ways to design and control collective behavior in synthetic systems, promising both deeper understanding of decision-driven collective phenomena and new possibilities for engineering complex systems with desired behaviors.

4. METHODS

A. Agent-based model

The agent-based model underlying the field equations (3) and (4) was chosen as a modified version of the minimal shepherding model considered in earlier work by some of the authors [37]. It involves all of the essential ingredients for shepherding dynamics and is, at the same time, particularly suitable for the derivation of field equations.

Specifically, we consider a binary mixture of mobile, disk-like agents of type T or H (with 2D Cartesian position vectors \mathbf{T}_a and \mathbf{H}_i , respectively) moving in a square box of side length L with periodic boundary conditions. We discuss here the case of a circular goal region around the origin; the case with a rectangular goal region, essentially representing a 1D problem, is discussed in Supplementary Information Section I.D.

The positions evolve in time according to overdamped Langevin dynamics, that is, both species are subject to Gaussian white noises representing the effects of (e.g., environmental or heterogeneity-induced) disorder on the coarse-grained scale (similar approaches were taken, e.g., in swarm robotics [72, 73], collective behaviours in biology [74, 75], and in crowd dynamics systems [76]). Further reasoning particularly for herder's noise is outlined in Supplementary Information Section I.A. We neglect inertial effects as it is often done in the robotics and control literature on shepherding [39, 77]. The targets' and herders' dynamics are given by

$$\dot{\mathbf{T}}_a = k^{\text{SR}} \left(\sum_{b \neq a}^{N_T} \mathbf{F}_{\text{SR}}^{\text{rep}}(\mathbf{T}_a, \mathbf{T}_b) + \sum_{i=1}^{N_H} \mathbf{F}_{\text{SR}}^{\text{rep}}(\mathbf{T}_a, \mathbf{H}_i) \right) + k^T \sum_{i=1}^{N_H} \mathbf{F}_{\text{LR}}^{\text{rep}}(\mathbf{T}_a, \mathbf{H}_i) + \sqrt{2D} \mathcal{N}_a \quad (7)$$

and

$$\dot{\mathbf{H}}_i k^{\text{SR}} \left(\sum_{j \neq i}^{N_H} \mathbf{F}_{\text{SR}}^{\text{rep}}(\mathbf{H}_i, \mathbf{H}_j) + \sum_{a=1}^{N_T} \mathbf{F}_{\text{SR}}^{\text{rep}}(\mathbf{H}_i, \mathbf{T}_a) \right) + k^H \mathbf{u}_i + \sqrt{2D} \mathcal{N}_i \quad (8)$$

respectively, where $\mathcal{N}_{a,i}$ are zero-mean white (i.e., delta-correlated) noises with unit variances, and the diffusion constants D are assumed to be equal. All agents interact through symmetric (reciprocal) short-range (SR) repulsive forces $\mathbf{F}_{\text{SR}}^{\text{rep}}$ of amplitudes $k^{\text{SR}} > 0$ and range σ , the latter representing the (uniform) particle diameter. In addition, the targets [see (7)] are subject to a long-range (LR) repulsive force $\mathbf{F}_{\text{LR}}^{\text{rep}}$ from the herders, with amplitude $k^T > 0$ and range $\lambda > \sigma$. The LR repulsion reflects the tendency of a target to escape from an approaching herder. For both, SR and LR types of repulsion, as is common in the Literature (e.g., [78, 79]), we assume a linearly decreasing dependence on the distance, such that, e.g.,

$$\mathbf{F}_{\text{LR}}^{\text{rep}}(\mathbf{T}_a, \mathbf{H}_i) = \frac{\mathbf{d}_{ai}}{|\mathbf{d}_{ai}|} (\lambda - d_{ij}) \Theta(\lambda - d_{ij}) \quad (9)$$

where $d_{ai} = |\mathbf{d}_{ai}| = |\mathbf{T}_a - \mathbf{H}_i|$, and $\Theta(x) = 1$ if $x > 0$, 0 otherwise. This linear ansatz is particularly useful for our later derivation of field equations [12]. For the SR repulsion we have the same functional form of the interaction, but the range λ is replaced by the particle diameter σ .

Beyond SR repulsion, the equation of the herders (8) contains the essential ingredient to realize shepherding, that is, the feedback control input \mathbf{u}_i defined in Eq. (2). As described in Sec. 1, the feedback term represents the (linear) attraction of a herder towards a strategic position behind its selected target. Specifically, this position is given by $\mathbf{T}_i^* + \delta \widehat{\mathbf{T}}_i^*$, where \mathbf{T}_i^* [see Eq. (1)] is the position of the selected target (within a sensing radius ξ and with selectivity γ), and $\delta \widehat{\mathbf{T}}_i^*$ represents a displacement along the target's position vector ($\widehat{\mathbf{T}}_i^*$ being the unit vector along \mathbf{T}_i^*). The parameter δ determines how far behind the target the herder should position itself to effectively steer the target's dynamics towards the origin. (As long as $0 < \delta < \lambda$ the herder can successfully navigate the selected target towards the origin.)

Equations (7), (8), combined with Eqs. (1) and (2), constitute the fundamental components of our agent-based model. A distinctive feature of these equations is that the coupling between targets and herders cannot be derived from a Hamiltonian and exhibits strong nonreciprocity in two key aspects: First, there is an inherent asymmetry in the interaction forces – targets experience repulsion from herders while herders are attracted to targets, which appears to violate Newton's third law (though this apparent contradiction is resolved when considering the coarse-grained nature of our description). Second, the selective nature of the herders' attraction introduces another form of nonreciprocity – herders interact only with specific targets chosen according to their selection rule and guide them toward the goal, whereas targets respond uniformly to all herders without any such selectivity.

To achieve effective confinement of targets (see Fig. 1), we assume that the sensing radius of the herders exceeds that of target-herder repulsion ($\xi > \lambda$), consistent with earlier literature [37, 39, 45]. Details of the simulations are provided in the subsequent paragraph 4 B 1.

B. Numerical calculations based on the agent-based model

1. Technical details

The simulations are performed in a square periodic box of size $L \times L$ with $L = 80\sigma$, where $\sigma = 1$ defines the particle diameter. The diffusion constant is set to $D = 1$, which characterizes the strength of noise in the system. Using the characteristic time scale $\tau = \sigma^2/D$, we employ a time step of $dt = 1 \cdot 10^{-3}\tau$. For initial conditions, we randomly and uniformly distribute $N_H = 400$ herders and $N_T = 400$ targets in the simulation box, resulting in equal initial densities of $\rho_0^T = \rho_0^H = 0.25/\sigma^2$ for both agent types (see Supplementary Information Section I.B for further details). The system typically reaches stationary states after a transient period of $t_{\text{tran}} = 200\tau$, and we run the simulations for a total duration of $t = 300\tau$.

Results for different values of the ratio N_H/N_T are reported in Supplementary Information Section I.C.

The agent-agent interactions are characterized by three distinct force contributions, each with specific parameters. For the short-range repulsive forces, which act between all agents regardless of type, we choose the particle diameter as $\sigma = 1$ and amplitude $k^{\text{SR}} = 100$. The long-range target-herder repulsion is characterized by an interaction radius $\lambda = 2.5$ and amplitude $k^T = 3$. The long-range herder attraction has a sensing radius $\xi = 5$ and force amplitude $k^H = 3$. The snapshots in Fig. 5(i-1) are obtained with the same numerical values, and with $\gamma = 5$ and $\delta = \lambda/2 = 1.25$; the dynamical equations are presented and discussed in Supplementary Information Section III.A.

2. Density profiles and order parameters

The radial density profiles $\hat{\rho}^T(r)$ and $\hat{\rho}^H(r)$ are computed by constructing histograms of the spatial distribution of targets and herders, respectively, as a function of their radial distance r from the origin. These profiles are obtained by time-averaging over an interval of $t_{\text{avg}} = 100\tau$ after the system has reached a steady state.

The radial densities are computed using an array of equispaced points from the origin to $L/2$ (half the box length), with a step size of $\Delta r = \xi/4$. The normalization of these density profiles follows the condition $\int_0^{L/2} \int_0^{2\pi} \hat{\rho}(r)r, drd\theta = \chi(L/2)$, where $\chi(L/2)$ represents the fraction of targets contained within a circle of radius $L/2$ centered at the origin. The profiles $\hat{\rho}^T(r)$ and $\hat{\rho}^H(r)$ are obtained by averaging over the polar angle θ , which is appropriate given our focus on the radial structure of the confined state. Final results are obtained by averaging over an ensemble of 48 independent simulations.

We now define the two order parameters χ and σ/Δ considered in Fig. 4. First, to retrieve information on the width of the target-herder interface, Δ , we fit the calculated density profile of the targets to a hyperbolic profile $\rho_f(r)$. This choice is inspired by theoretical studies on the vapor-liquid interface in phase-separating fluids [80]. The explicit expression for $\rho_f(r)$ is given by

$$\rho_f(r) = \rho_f(r; c, R, \Delta) = \frac{c}{2} \left(1 - \tanh \left(\frac{x - R}{\Delta} \right) \right) \quad (10)$$

where c , R , Δ are the fitting parameters representing, respectively, the maximum values of the profile, the position of the interface, and its width. We use the inverse of the width, σ/Δ , as an estimate of the sharpness of the target-herder interface.

The confinement order parameter $\chi(R)$ measures the fraction of targets located within a distance R from the origin. In Fig. 4, the reference radius R is chosen as the fitting parameter R of the density profile obtained at maximum values of γ and δ , where the spatial segregation between targets and herders is most distinct. In this case, the spatial separation between targets and herders is most pronounced. The quantity χ is then calculated by averaging the instantaneous fraction of targets inside a circle of radius R , both over time ($t_{\text{avg}} = 100\tau$) and over an ensemble of 48 independent simulations. In Supplementary Information Section I.E we show that different choices of R do not impact the qualitative behaviour of our results.

C. Derivation of the field equations

Starting from the agent-based stochastic equations (7), (8) we now derive corresponding partial differential equations (PDEs) describing the spatial-temporal dynamics of the two density fields $\rho^{T(H)}$. The final structure of these equations is given in Eqs. (3) and (4). As in Sec. 2A we consider 1-dimensional dynamics along the x -direction; the derivation can be easily generalized to higher dimensions.

Due to the conservation of the number of particles, both density fields $\rho^{T(H)}(x, t) = \sum_{a(i)=1}^{N^{T(H)}} \delta(x - x_{i(a)}^{T(H)}(t))$ obey a continuity equation, that is,

$$\partial_t \rho^{T(H)}(x, t) = \nabla \cdot j^{T(H)}(x, t) + D \nabla^2 \rho^{T(H)}(x, t) \quad (11)$$

where $\nabla = \partial/\partial x$ and the currents $j^{T(H)}(x, t)$ take into account the various force terms in Eqs. (7), (8).

The (piecewise linear) pair forces comprising the (SR or LR) repulsion in Eqs. (7) and (8) can be handled straightforwardly [12] (see Supplementary Information Section 2.A for details). Here we sketch the main idea. Each of the pair terms is of the form $F_i = \sum_{j=1}^M F_{ij}$, where M is the number of interacting neighbors. Under a mean field assumption, F_i gives rise to an average force that, when neglecting nontrivial spatio-temporal correlations, has the form $\langle F(x, t) \rangle = \int F(x, y) \rho(y, t) dy$ where the integral extends over the interaction zone around x . For both the SR and LR forces, $F(x, y)$ represents a *translationally invariant* kernel, i.e., $F(x, y) = F(x - y)$. The resulting contribution to the current then has the form $-\langle F \rangle(x, t) \rho(x, t)$. To compute the integrals in $\langle F \rangle$, we perform a gradient expansion of $\rho(y, t)$ around x , i.e., $\rho(y) = \rho(x) + \nabla \rho(x)(y - x) + \mathcal{O}(\nabla \rho^2)$. Zeroth-order terms vanish due to translational invariance of the kernel. Keeping only linear terms in the gradients, we obtain the following currents stemming from repulsive forces

$$\begin{aligned} j_{\text{rep}}^T(x, t) &= \rho^T(x, t) (\alpha^{\text{SR}} \nabla \rho^{\text{tot}}(x, t) + \alpha^{\text{LR}} \nabla \rho^T(x, t)) \\ j_{\text{rep}}^H(x, t) &= \rho^H(x, t) \alpha^{\text{SR}} \nabla \rho^{\text{tot}}(x, t) \end{aligned} \quad (12)$$

where $\rho^{\text{tot}}(x, t) = \rho^T(x, t) + \rho^H(x, t)$ is the combined density field, and $\alpha^{\text{SR}} = k^{\text{SR}} \sigma^3 / 3$ and $\alpha^{\text{LR}} = k^T \lambda^3 / 3$ are positive constants related to the respective interaction radii and coupling constants in Eqs. (7), (8).

With careful consideration, the third term on the right side of Eq.(8), which describes herders' decision-making abilities, can also be handled using a mean-field-like approach and a density gradient expansion. This term depends on two key components defined in previous equations: the feedback control input \mathbf{u}_i [Eq. (2)] and the position of the selected target \mathbf{T}_i^* [Eq. (1)]. Unlike typical classical systems where forces have a pairwise character, the resulting "force" here represents a three-body coupling between the herder's position, the selected target's position, and the origin. This leads to a mean-field force $\langle F(x, t) \rangle = \int F(x, y) \rho(y, t) dy$ with a kernel that lacks translational invariance and depends nonlinearly on both coordinates x and y . To proceed, we (i) linearize the (exponential) weight function appearing in the numerator of Eq. (2) (valid for $\gamma \lesssim 1/\xi$), and (ii) neglect the denominator. The kernel can then be expressed as

$$F(x, y) = -k^H (1 + \gamma(|y| - |x|))(x - (y + \text{sign}(y)\delta)) \quad (13)$$

This simplified form where the selection rule has been linearized in x and y , still lacks translational invariance. A notable consequence is that even the zeroth-order term in the gradient expansion of $\rho^T(y)$ around $\rho^T(x)$ contributes to the average force. Combining this with the first-order (linear) gradient term, we obtain the following expression for finite values of the decision-making parameters γ and δ :

$$j_{\text{dm}}^H(x, t) = -g_1(x; \gamma, \delta) \rho^H(x, t) \rho^T(x, t) - g_2(x; \gamma, \delta) \rho^H(x, t) \nabla \rho^T(x, t). \quad (14)$$

Here, $g_{1/2}(x; \gamma, \delta)$ are space-dependent functions whose explicit expression is given by

$$g_1(\gamma, \delta, x) = \text{sign}(x) \begin{cases} 2\delta\xi + \frac{2}{3}\gamma\xi^3, & \xi \leq |x| \leq L/2 - \xi \\ \left[\delta(1 - 2\gamma|x|)(|x| - \xi) + \delta(|x| + \xi) + \gamma x(\xi^2 - x^2) + \frac{2}{3}\gamma|x|^3 \right], & |x| < \xi \\ \left[\delta(1 - 2\gamma(L/2 - |x|))((L/2 - |x|) - \xi) + \delta((L/2 - |x|) + \xi) \right. \\ \left. + \gamma(L/2 - |x|)(\xi^2 - (L/2 - |x|)^2) + \frac{2}{3}\gamma(L/2 - |x|)^3 \right], & |x| > L/2 - \xi \end{cases} \quad (15)$$

$$g_2(\gamma, \delta, x) = \begin{cases} \frac{2}{3}(\delta\gamma + 1)\xi^3, & \xi \leq |x| \leq L/2 - \xi \\ \left[\delta(1 - \gamma|x|)(\xi^2 - x^2) + \frac{2\xi^3}{3}(\delta\gamma + 1) - \frac{2}{3}(\gamma|x|)(\xi^3 - |x|^3) + \left(\frac{\gamma}{2}\right)(\xi^4 - x^4) \right], & |x| < \xi \\ \left[\delta(1 - \gamma(L/2 - |x|))(\xi^2 - (L/2 - |x|)^2) + \frac{2\xi^3}{3}(\delta\gamma + 1) \right. \\ \left. - \frac{2}{3}(\gamma(L/2 - |x|))(\xi^3 - (L/2 - |x|)^3) + \left(\frac{\gamma}{2}\right)(\xi^4 - (L/2 - |x|)^4) \right], & |x| > L/2 - \xi \end{cases} \quad (16)$$

Note that the functions v_1 and v_2 in (4) are scaled versions of g_1 and g_2 . For further details on the derivation of $j_{\text{dm}}^{\text{H}}(x, t)$ see Supplementary Information Section II.A. Figure 2(a) illustrates the behavior of v_1 and v_2 . The consistently positive values of v_2 across all positions demonstrate the attractive force that targets exert on the herders. In contrast to v_2 , function v_1 changes its sign at $x = 0$, with positive (negative) values at positive (negative) values of x . The resulting current acting on the herders thus depends on *where* these targets are relative to the goal region, consistent with our decision-making strategy. We stress that such a term is absent in more conventional nonreciprocal field theories of mixtures, e.g., the Cahn-Hilliard model [12].

In the special case $\gamma = \delta = 0$ (no target selection and no trajectory planning) these functions reduce to the constants $g_1 = 0$ and $g_2 = g_2^0$ with $g_2^0 = 2k^{\text{H}}\xi^3/3 > 0$, yielding the current

$$j_{\text{dm}}^{\text{H}}(x, t)|_{\gamma=\delta=0} = -g_2^0\rho^{\text{H}}(x, t)\nabla\rho^{\text{T}}(x, t) \quad (17)$$

Note that, even in this "uncontrolled" case, where herders are unable to make decisions, the resulting field equations (11) for the two density field are nonreciprocal due to the different signs and values of the cross coupling terms, as are the corresponding Langevin equations (7), (8) in this limit.

Finally, inserting the currents (12) and (14) into the continuity equations (11) we obtain the PDEs

$$\partial_t\rho^{\text{T}} = \nabla \cdot [\rho^{\text{T}}((\alpha^{\text{SR}}\nabla\rho^{\text{tot}} + \alpha^{\text{LR}}\nabla\rho^{\text{T}})] + D\nabla^2\rho^{\text{T}} \quad (18)$$

and

$$\partial_t\rho^{\text{H}} = \nabla \cdot [\rho^{\text{H}}\alpha^{\text{SR}}\nabla\rho^{\text{tot}} - g_1(x; \gamma, \delta)\rho^{\text{T}}\rho^{\text{H}} - g_2(x; \gamma, \delta)\rho^{\text{H}}\nabla\rho^{\text{T}}] + D\nabla^2\rho^{\text{H}} \quad (19)$$

where we have omitted the arguments of the density fields. We non-dimensionalize these equations by choosing the Brownian time, $\tau \equiv \sigma^2/D$, as characteristic time scale and the particle diameter, σ , as characteristic length scale. Densities are scaled with the overall density $\rho_0 = (N_{\text{T}} + N_{\text{H}})/L$. We further introduce dimensionless and renormalized diffusion coefficients $D^{\text{A}}(\rho^{\text{A}}) = D\frac{\tau}{\sigma^2} + \alpha^{\text{SR}}\frac{\tau\rho_0}{\sigma^2}\rho^{\text{A}}$ with $\text{A} = \{\text{T}, \text{H}\}$, which describe both, the effect of the noise and the intra-species short-range (SR) repulsion. With $\tilde{k}^{\text{T}} \equiv \alpha^{\text{LR}}\frac{\tau\rho_0}{\sigma^2}$, $v_1 \equiv g_2\frac{\tau\rho_0}{\sigma}$, and $v_2 = g_2\frac{\tau\rho_0}{\sigma^2}$ (and $v_2^0 = g_2^0\frac{\tau\rho_0}{\sigma^2}$), we then arrive at the field equations given in (3) and (4).

D. Numerical calculations in continuum

The partial differential equations are integrated using a pseudospectral code combined with an operator splitting technique [81], which allows to accurately treat the linear part of the spatial operator (the linear diffusion). The non-linear parts of the spatial operator (non reciprocal interactions and reciprocal SR repulsion) are treated as source terms: at every time-step, they are evaluated in real space using the values from the previous step. Then they are transformed into the Fourier space, where they are considered as source terms and integrated using a fourth-order Runge-Kutta time integration scheme.

In the actual calculations, the periodically repeated, one-dimensional segment $[-L, L] \subset \mathbb{R}$ with $L = 40\sigma$ is divided into $N = 201$ equispaced grid points. The time step is chosen as $dt = 1 \cdot 10^{-4}\tau$. The simulations are run for a total duration of $t = 150\tau$, which is sufficient to reach a steady state. For Fig. 5(h), $dt = 1 \cdot 10^{-3}\tau$, $t = 750\tau$. The initial conditions are assumed to be slightly perturbed disordered states with $\rho_0^T = \rho_0^H = \rho_0/2 = 0.25$.

In our continuum model, most parameters can be directly adopted from the considered agent-based simulation parameters. Exceptions are, first, the sensing radius ξ which we set to $\xi = 2.5\sigma$ to mitigate the effects of neglecting the denominator in Eq. (1). Second, the diffusion constant D is set to $D = 5$ to increase numerical stability. Third, the amplitude of the short-range repulsion is set to $k^{\text{SR}} = 75$ so that $v_2^0 > 0$. To reproduce Fig. 2(b, d) we set $\gamma = 2.5$, $\delta = \lambda/2$. To reproduce Fig. 5(i-1), we set $v_2(x) = \tilde{v}_2 = \text{const}$, while $v_1(x)$ is described by a square wave with different periods and amplitude \tilde{v}_1 (details are given in the Supplementary Information Section III.A). Specifically, we set $\tilde{v}_1 = k^H(2\delta\xi + (2/3)\gamma(\xi^3))(\sigma/D)\rho_0$ and $\tilde{v}_2 = k^H(2/3)(\delta\gamma + 1)(\xi^3)(\rho_0/D)$, which would be the (constant) absolute values of $v_1(x)$ and $v_2(x)$ in the range $\xi \leq |x| \leq L/2 - \xi$; within these expressions, we set $\gamma = 2.5$, $\delta = \lambda/2$. Only to reproduce Fig. 5(h) we use $k^T = 10$, while for remaining part of the manuscript, $k^T = 3$.

The order parameters are calculated in analogy to the corresponding agent-based calculations; see Sec. 4B2. For the quantity $\chi(R)$, we use the definition $\chi(R) = \frac{1}{\mathcal{C}} \int_{-R}^{R^*} \rho^T(x) dx$, with \mathcal{C} being a proper normalization factor.

DATA AVAILABILITY

The authors declare that the data supporting the findings of this study are available within the paper and its Supplementary Information files or from the corresponding author on reasonable request.

ACKNOWLEDGEMENTS

MdB and AL wish to acknowledge support from the MUR (Italian Ministry of University and Research) Research project ‘‘Machine-learning based control of complex multi-agent systems for search and rescue operations in natural disasters’’ (MENTOR) – [PRIN 2022 – CUP: E53D23001160006 – SETTORE ERC PE7] and funding from the Scuola Superiore Meridionale in Naples, Italy which supported AL visit to TUB.

5. AUTHOR CONTRIBUTIONS

SK, MdB and AL jointly conceived and designed the research; AL wrote and checked the numerical code, carried out the derivations and data analysis with inputs from SK and MdB. All authors contributed to the analysis and interpretation of the results and were involved with the writing of the manuscript.

COMPETING INTERESTS

The authors declare no competing interests.

-
- [1] D. J. Sumpter, *Collective animal behavior* (Princeton University Press, 2010).
- [2] M. Ballerini, N. Cabibbo, R. Candelier, A. Cavagna, E. Cisbani, I. Giardina, V. Lecomte, A. Orlandi, G. Parisi, A. Proccacci, *et al.*, Interaction ruling animal collective behavior depends on topological rather than metric distance: Evidence from a field study, *Proceedings of the national academy of sciences* **105**, 1232 (2008).
- [3] K. Kuru, Planning the future of smart cities with swarms of fully autonomous unmanned aerial vehicles using a novel framework, *IEEE Access* **9**, 6571 (2021).
- [4] M. Brambilla, E. Ferrante, M. Birattari, and M. Dorigo, Swarm robotics: a review from the swarm engineering perspective, *Swarm Intelligence* **7**, 1 (2013).
- [5] F. Bullo, J. Cortés, and S. Martinez, *Distributed control of robotic networks: a mathematical approach to motion coordination algorithms*, Vol. 27 (Princeton University Press, 2009).
- [6] S. Nagel, J. Heitzig, and E. Schöll, Macroscopic stochastic model for economic cycle dynamics, *Phys. Rev. Lett.* **134**, 047402 (2025).
- [7] R. M. D'Souza, M. di Bernardo, and Y.-Y. Liu, Controlling complex networks with complex nodes, *Nature Reviews Physics* **5**, 250 (2023).
- [8] P. C. Hohenberg and B. I. Halperin, Theory of dynamic critical phenomena, *Rev. Mod. Phys.* **49**, 435 (1977).
- [9] M. C. Cross and P. C. Hohenberg, Pattern formation outside of equilibrium, *Rev. Mod. Phys.* **65**, 851 (1993).
- [10] M. C. Marchetti, J.-F. Joanny, S. Ramaswamy, T. B. Liverpool, J. Prost, M. Rao, and R. A. Simha, Hydrodynamics of soft active matter, *Rev. Mod. Phys.* **85**, 1143 (2013).
- [11] J.-F. Joanny, Active behavior of the cytoskeleton, *Physics reports* **449**, 3 (2007).
- [12] Z. You, A. Baskaran, and M. C. Marchetti, Nonreciprocity as a generic route to traveling states, *Proceedings of the National Academy of Sciences* **117**, 19767 (2020).
- [13] M. Fruchart, R. Hanai, P. B. Littlewood, and V. Vitelli, Non-reciprocal phase transitions, *Nature* **592**, 363 (2021).
- [14] L. Xiong, Y. Cao, R. Cooper, W.-J. Rappel, J. Hasty, and L. Tsimring, Flower-like patterns in multi-species bacterial colonies, *eLife* **9**, e48885 (2020).
- [15] E. Theveneau, B. Steventon, E. Scarpa, S. Garcia, X. Trepas, A. Streit, and R. Mayor, Chase-and-run between adjacent cell populations promotes directional collective migration, *Nat. Cell Biol.* **15**, 763 (2013).
- [16] C. H. Meredith, P. G. Moerman, J. Groenewold, Y.-J. Chiu, W. K. Kegel, A. van Blaaderen, and L. D. Zarzar, Predator-prey interactions between droplets driven by non-reciprocal oil exchange, *Nat. Chem.* **12**, 1136 (2020).
- [17] A. V. Ivlev, J. Bartnick, M. Heinen, C.-R. Du, V. Nosenko, and H. Löwen, Statistical mechanics where Newton's third law is broken, *Phys. Rev. X* **5**, 011035 (2015).
- [18] S. Saha, S. Ramaswamy, and R. Golestanian, Pairing, waltzing and scattering of chemotactic active colloids, *New J. Phys.* **21**, 063006 (2019).
- [19] M. A. Tsyganov, J. Brindley, A. V. Holden, and V. N. Biktashev, Quasisoliton interaction of pursuit-evasion waves in a predator-prey system, *Phys. Rev. Lett.* **91**, 218102 (2003).
- [20] F. A. Lavergne, H. Wendeheine, T. Bäuerle, and C. Bechinger, Group formation and cohesion of active particles with visual perception-dependent motility, *Science* **364**, 70 (2019).
- [21] S. A. M. Loos, S. H. L. Klapp, and T. Martynek, Long-range order and directional defect propagation in the nonreciprocal XY model with vision cone interactions, *Phys. Rev. Lett.* **130**, 198301 (2023).
- [22] H. Sompolinsky and I. Kanter, Temporal association in asymmetric neural networks, *Phys. Rev. Lett.* **57**, 2861 (1986).
- [23] H. Hong and S. H. Strogatz, Kuramoto model of coupled oscillators with positive and negative coupling parameters: An example of conformist and contrarian oscillators, *Phys. Rev. Lett.* **106**, 054102 (2011).
- [24] D. Helbing and P. Molnár, Social force model for pedestrian dynamics, *Phys. Rev. E* **51**, 4282 (1995).
- [25] A. Metelmann and A. A. Clerk, Nonreciprocal photon transmission and amplification via reservoir engineering, *Phys. Rev. X* **5**, 021025 (2015).
- [26] S. Zhang, Y. Hu, G. Lin, Y. Niu, K. Xia, J. Gong, and S. Gong, Thermal-motion-induced non-reciprocal quantum optical system, *Nat. Photonics* **12**, 744 (2018).
- [27] A. McDonald, R. Hanai, and A. A. Clerk, Nonequilibrium stationary states of quantum non-Hermitian lattice models, *Phys. Rev. B* **105**, 064302 (2022).
- [28] M. Reisenbauer, H. Rudolph, L. Egyed, K. Hornberger, A. V. Zasedatelev, M. Abuzarli, B. A. Stickler, and U. Delić, Non-Hermitian dynamics and non-reciprocity of optically coupled nanoparticles, *Nat. Phys.* **20**, 1629 (2024).
- [29] V. Liška, T. Zemánková, P. Ják, M. Šiler, S. H. Simpson, P. Zemánek, and O. Brzobohatý, Pt-like phase transition and limit cycle oscillations in non-reciprocally coupled optomechanical oscillators levitated in vacuum, *Nat. Phys.* **20**, 1622 (2024).
- [30] S. Saha, J. Agudo-Canalejo, and R. Golestanian, Scalar active mixtures: The nonreciprocal cahn-hilliard model, *Physical Review X* **10**, 041009 (2020).
- [31] A. Dinelli, J. O'Byrne, A. Curatolo, Y. Zhao, P. Sollich, and J. Tailleur, Non-reciprocity across scales in active mixtures, *Nat. Commun.* **14**, 7035 (2023).
- [32] T. Frohoff-Hülsmann and U. Thiele, Nonreciprocal Cahn-Hilliard model emerges as a universal amplitude equation, *Phys. Rev. Lett.* **131**, 107201 (2023).
- [33] F. Brauns and M. C. Marchetti, Nonreciprocal pattern formation of conserved fields, *Physical Review X* **14**, 021014 (2024).

- [34] T. Suchanek, K. Kroy, and S. A. M. Loos, Irreversible mesoscale fluctuations herald the emergence of dynamical phases, *Phys. Rev. Lett.* **131**, 258302 (2023).
- [35] K. L. Kreienkamp and S. H. L. Klapp, Nonreciprocal alignment induces asymmetric clustering in active mixtures, *Phys. Rev. Lett.* **133**, 258303 (2024).
- [36] C. Scheibner, A. Souslov, D. Banerjee, P. Surówka, W. T. Irvine, and V. Vitelli, Odd elasticity, *Nature Physics* **16**, 475 (2020).
- [37] A. Lama and M. di Bernardo, Shepherding and herdability in complex multiagent systems, *Physical Review Research* **6**, L032012 (2024).
- [38] P. Nalepka, R. W. Kallen, A. Chemero, E. Saltzman, and M. J. Richardson, Herd those sheep: Emergent multiagent coordination and behavioral-mode switching, *Psychological science* **28**, 630 (2017).
- [39] S. Zhang, X. Lei, M. Duan, X. Peng, and J. Pan, A distributed outmost push approach for multirobot herding, *IEEE Transactions on Robotics* **40**, 1706 (2024).
- [40] A. Attanasi, A. Cavagna, L. Del Castello, I. Giardina, T. S. Grigera, A. Jelić, S. Melillo, L. Parisi, O. Pohl, E. Shen, *et al.*, Information transfer and behavioural inertia in starling flocks, *Nature physics* **10**, 691 (2014).
- [41] D. Ko and E. Zuazua, Asymptotic behavior and control of a “guidance by repulsion” model, *Mathematical Models and Methods in Applied Sciences* **30**, 765 (2020).
- [42] Y.-Y. Liu, J.-J. Slotine, and A.-L. Barabási, Controllability of complex networks, *nature* **473**, 167 (2011).
- [43] A. Krizhevsky, I. Sutskever, and G. E. Hinton, Imagenet classification with deep convolutional neural networks, *Advances in neural information processing systems* **25** (2012).
- [44] S. Van Havermaet, P. Simoens, T. Landgraf, and Y. Khaluf, Steering herds away from dangers in dynamic environments, *Royal Society Open Science* **10**, 230015 (2023).
- [45] F. Auletta, D. Fiore, M. J. Richardson, and M. di Bernardo, Herding stochastic autonomous agents via local control rules and online target selection strategies, *Autonomous Robots* **46**, 469 (2022).
- [46] A. V. Ivlev, J. Bartnick, M. Heinen, C.-R. Du, V. Nosenko, and H. Löwen, Statistical mechanics where newton’s third law is broken, *Physical Review X* **5**, 011035 (2015).
- [47] M. Fruchart, R. Hanai, P. B. Littlewood, and V. Vitelli, Non-reciprocal phase transitions, *Nature* **592**, 363 (2021).
- [48] A. Giusti, G. C. Maffettone, D. Fiore, M. Coraggio, and M. di Bernardo, Distributed control for geometric pattern formation of large-scale multirobot systems, *Frontiers in Robotics and AI* **10**, 1219931 (2023).
- [49] C. Liu, X. Fu, L. Liu, X. Ren, C. K. Chau, S. Li, L. Xiang, H. Zeng, G. Chen, L.-H. Tang, *et al.*, Sequential establishment of stripe patterns in an expanding cell population, *Science* **334**, 238 (2011).
- [50] X. Fu, L.-H. Tang, C. Liu, J.-D. Huang, T. Hwa, and P. Lenz, Stripe formation in bacterial systems with density-suppressed motility, *Physical review letters* **108**, 198102 (2012).
- [51] J. A. Sherratt and M. J. Smith, Periodic travelling waves in cyclic populations: field studies and reaction–diffusion models, *Journal of the Royal Society Interface* **5**, 483 (2008).
- [52] M. A. Haque, A. R. Rahmani, and M. B. Egerstedt, Biologically inspired confinement of multi-robot systems, *International Journal of Bio-Inspired Computation* **3**, 213 (2011).
- [53] P. Domenici, R. S. Batty, T. Similä, and E. Ogam, Killer whales (*orcinus orca*) feeding on schooling herring (*clupea harengus*) using underwater tail-slaps: kinematic analyses of field observations, *Journal of Experimental Biology* **203**, 283 (2000).
- [54] S. Lemoine, C. Boesch, A. Preis, L. Samuni, C. Crockford, and R. M. Wittig, Group dominance increases territory size and reduces neighbour pressure in wild chimpanzees, *Royal Society Open Science* **7**, 200577 (2020).
- [55] S. G. Prasath, S. Mandal, F. Giardina, J. Kennedy, V. N. Murthy, and L. Mahadevan, Dynamics of cooperative excavation in ant and robot collectives, *Elife* **11**, e79638 (2022).
- [56] H. Rainer and U. Krause, Opinion dynamics and bounded confidence: Models, analysis and simulation, *Journal of Artificial Societies and Social Simulation* **5** (2002).
- [57] N. Masuda, Opinion control in complex networks, *New Journal of Physics* **17**, 033031 (2015).
- [58] P. Nalepka, M. Lamb, R. W. Kallen, K. Shockley, A. Chemero, E. Saltzman, and M. J. Richardson, Human social motor solutions for human-machine interaction in dynamical task contexts, *Proc Natl Acad Sci U S A* **116**, 1437 (2019).
- [59] N. Long, K. Sammut, D. Sgarioto, M. Garratt, and H. Abbass, A comprehensive review of shepherding as a bio-inspired swarm-robotics guidance approach], *IEEE Transactions on Emerging Topics in Computational Intelligence* **4**, 523 (2020).
- [60] M. M. Norton, P. Grover, M. F. Hagan, and S. Fraden, Optimal control of active nematics, *Physical review letters* **125**, 178005 (2020).
- [61] L. K. Davis, K. Proesmans, and É. Fodor, Active matter under control: Insights from response theory, *Physical Review X* **14**, 011012 (2024).
- [62] U. Khadka, V. Holubec, H. Yang, and F. Cichos, Active particles bound by information flows, *Nature communications* **9**, 3864 (2018).
- [63] R. C. Löffler, E. Panizon, and C. Bechinger, Collective foraging of active particles trained by reinforcement learning, *Scientific Reports* **13**, 17055 (2023).
- [64] M. Nasiri and B. Liebchen, Reinforcement learning of optimal active particle navigation, *New Journal of Physics* **24**, 073042 (2022).
- [65] D. Levis, A. Diaz-Guilera, I. Pagonabarraga, and M. Starnini, Flocking-enhanced social contagion, *Physical Review Research* **2**, 032056 (2020).

- [66] D. Levis, I. Pagonabarraga, and A. Díaz-Guilera, Synchronization in dynamical networks of locally coupled self-propelled oscillators, *Physical Review X* **7**, 011028 (2017).
- [67] R. A. Licitra, Z. I. Bell, and W. E. Dixon, Single-agent indirect herding of multiple targets with uncertain dynamics, *IEEE Transactions on Robotics* **35**, 847 (2019).
- [68] R. Supekar, B. Song, A. Hastewell, G. P. T. Choi, A. Mietke, and J. Dunkel, Learning hydrodynamic equations for active matter from particle simulations and experiments, *Proceedings of the National Academy of Sciences* **120**, e2206994120 (2023), <https://www.pnas.org/doi/pdf/10.1073/pnas.2206994120>.
- [69] G. C. Maffettone, A. Boldini, M. Di Bernardo, and M. Porfiri, Continuification control of large-scale multiagent systems in a ring, *IEEE Control Systems Letters* **7**, 841 (2022).
- [70] R. Supekar, B. Song, A. Hastewell, G. P. Choi, A. Mietke, and J. Dunkel, Learning hydrodynamic equations for active matter from particle simulations and experiments, *Proceedings of the National Academy of Sciences* **120**, e2206994120 (2023).
- [71] A. Ziepke, I. Maryshev, I. S. Aranson, and E. Frey, Multi-scale organization in communicating active matter, *Nature communications* **13**, 6727 (2022).
- [72] G. Sartoretti, M.-O. Hongler, M. E. de Oliveira, and F. Mondada, Decentralized self-selection of swarm trajectories: from dynamical systems theory to robotic implementation, *Swarm Intelligence* **8**, 329 (2014).
- [73] G. Vásárhelyi, C. Virágh, G. Somorjai, T. Nepusz, A. E. Eiben, and T. Vicsek, Optimized flocking of autonomous drones in confined environments, *Science Robotics* **3**, eaat3536 (2018).
- [74] G. Ariel and A. Ayali, Locust collective motion and its modeling, *PLOS computational Biology* **11**, e1004522 (2015).
- [75] A. Cavagna, A. Culla, X. Feng, I. Giardina, T. S. Grigera, W. Kion-Crosby, S. Melillo, G. Pisegna, L. Postiglione, and P. Villegas, Marginal speed confinement resolves the conflict between correlation and control in collective behaviour, *Nature Communications* **13**, 2315 (2022).
- [76] S. Heliövaara, T. Korhonen, S. Hostikka, and H. Ehtamo, Counterflow model for agent-based simulation of crowd dynamics, *Building and Environment* **48**, 89 (2012).
- [77] E. Sebastián, E. Montijano, and C. Sagüés, Adaptive multirobot implicit control of heterogeneous herds, *IEEE Transactions on Robotics* **38**, 3622 (2022).
- [78] P. Dolai, A. Simha, and S. Mishra, Phase separation in binary mixtures of active and passive particles, *Soft Matter* **14**, 6137 (2018).
- [79] K. L. Kreienkamp and S. H. L. Klapp, Clustering and flocking of repulsive chiral active particles with non-reciprocal couplings, *New Journal of Physics* **24**, 123009 (2022).
- [80] The nature of the liquid-vapour interface and other topics in the statistical mechanics of non-uniform, classical fluids, *Advances in physics* **28**, 143 (1979).
- [81] C. Canuto, M. Y. Hussaini, A. Quarteroni, and T. A. Zang, *Spectral methods*, Vol. 285 (Springer, 2006).

Supplemental material for “An interpretable continuum framework for decision-making: nonreciprocal field theory of the herding control problem”

Andrea Lama*

Modeling and Engineering Risk and Complexity, Scuola Superiore Meridionale, Naples, 80125, Italy

Mario di Bernardo†

Department of Electrical Engineering and ICT, University of Naples Federico II, Naples, 80125, Italy

Sabine. H. L. Klapp‡

Institute for Theoretical Physics, Sec. EW 7-1, Technical University Berlin, Hardenbergstrasse 36, 10623 Berlin, Germany

(Dated: March 4, 2025)

In this Supplemental Information we provide, first, background information and additional results for our agent-based model. Second, we discuss several aspects of the continuum model regarding, in particular, the derivation and the linear stability analysis. Third, we discuss relations between continuum and agent-based results used in the context of the more general design rules considered in Fig. 5 of the main text. Finally, we present a list of the supplementary videos. A list of references list is given at the end of this Supplemental Information.

CONTENTS

I. Agent-based model	2
A. Comparison with other models	2
B. Guidelines for parameter choices	2
C. Impact of the number of herders	2
D. Impact of the geometry of the goal region	3
E. Robustness of results for the fraction of confined targets	4
II. Continuum theory	5
A. Derivation of coupling functions	5
1. Higher order terms in the gradient expansion	7
B. Analysis in the absence of decision-making	7
C. Sharpness of the herder-target interface	9
III. Pattern design beyond simple containment	10
A. Continuum: choices for $v_1(x)$	10
B. Agent dynamics: decision-making rules	12
C. Linear stability analysis for the case of constant coefficients \tilde{v}_1 and \tilde{v}_2	14
IV. List of Supplementary videos	16
References	16

* andrea.lama-ssm@unina.it

† mario.dibernardo@unina.it

‡ sabine.klapp@tu-berlin.de

I. AGENT-BASED MODEL

A. Comparison with other models

In this section we discuss our agent-based model (see Methods) in the light of earlier models describing shepherding dynamics, particularly the one considered by some of the authors in [1]. The latter model, along with other established ones [2–4], includes elements that are plausible on the microscopic level but make the derivation of a continuum theory unnecessarily complicated. It is for this reason that we have chosen here to simplify the model. The specific modifications compared to [1] are as follows:

First, and most importantly, we have removed a cooperation strategy between herders that prevents two or more of them to chase the same target. We recall [see Eq. (1) of the main text] that a herder i at position \mathbf{H}_i only considers targets a at positions \mathbf{T}_a within its sensing radius ξ (i.e., $|\mathbf{H}_i - \mathbf{T}_a| \leq \xi$). Ref. [1] additionally involves a proximity-based rule: even if another target b at \mathbf{T}_b is within herder i 's sensing region, it will not be followed by the herder i if there is another herder j (inside herder i 's sensing region) that is closer to b (i.e., if $|\mathbf{H}_j - \mathbf{T}_b| < |\mathbf{H}_i - \mathbf{T}_b|$). This mechanism promotes the desired pattern, namely a spreading of herders around the circular arrangement of targets, but is hard to translate to the continuum level. Upon removing this cooperative element, multiple herders can cluster around the same target that locally maximizes its distance from the origin. To qualitatively reproduce the herder spreading behavior, we introduce noise into the herders' dynamics – an element absent in earlier works [1–4]. For simplicity, we apply the same noise term used for target dynamics (see Eqs. (7-8) in the Methods). This noise mitigates the tendency of herders to cluster while chasing the same target; this partially recreates the desired spreading behavior. At the same time, the noise can be easily translated to the continuum by a diffusive term. We note that the introduction of noise within herder dynamics is not uncommon; it also used, e.g., to model environmental disturbances in collective animal behavior [5, 6] or measurement errors in swarm robotics [7, 8].

As a second modification compared to [1], we have eliminated the saturation of the herder speed, $\dot{\mathbf{H}}_i$, that was implemented in [1] to prevent unrealistically high values when varying the herders' sensing radius ξ over more than an order of magnitude. In the present work, ξ was fixed to a moderate value, making the saturation redundant.

Finally, we here employ a finite simulation box with periodic boundary conditions, consistent with the large body of literature in active and nonreciprocal systems (see, e.g., [9]). Given the presence of a "special" point being the center of the goal region, the resulting system can be visualized as a torus with one special point (i.e., the origin).

B. Guidelines for parameter choices

Equations (7-8) of the Methods contain multiple parameters that we have fixed based on the following considerations.

The domain size L and number of targets N_T were chosen to ensure the average target density $(N_T)/L^2$ remains sufficiently high to prevent issues arising from herders' limited sensing capabilities. This is achieved by maintaining N_T above the critical threshold $N_T^{\text{low}}(L, \xi)$ described in [1].

Following standard practices in control and robotics literature [10], we set the herder sensing radius ξ larger than the target repulsion range λ (i.e., $\xi > \lambda$). Additionally, we ensure that target-herder nonreciprocal interactions dominate over noise effects by maintaining $k^T \lambda^2 \gg D$ and $k^H \xi \gg D$. The soft, reciprocal, short-range repulsion is configured to dominate other interactions ($k^{\text{rep}} \gg k^H, k^T$) while maintaining the hierarchy of ranges, $\sigma < \lambda < \xi$. The concrete values for these parameters are given in the Methods.

C. Impact of the number of herders

The numerical results in the main text have been obtained by choosing equal numbers of targets and herders, that is, $N_T = N_H = 400$. Here we present results for systems where $N_H < N_T$, which is the common choice in the control literature on shepherding [1, 4, 11]. Figure S1 shows representative long-time configurations for different values of the control parameters γ and δ and $N_H = 100$ (panel (a)-(d)) and $N_H = 200$ (panel (e-h)), while $N_T = 400$ is fixed. Visual inspection of the respective snapshots suggests that the qualitative features of the dynamics observed for $N_H = 400$ (see Fig. 3 of the main text) remain. This robustness is further confirmed by the radial density profiles $\hat{\rho}^T(r)$ and $\hat{\rho}^H(r)$ shown in the insets, which exhibit spatial structures similar to those observed in our main analysis.

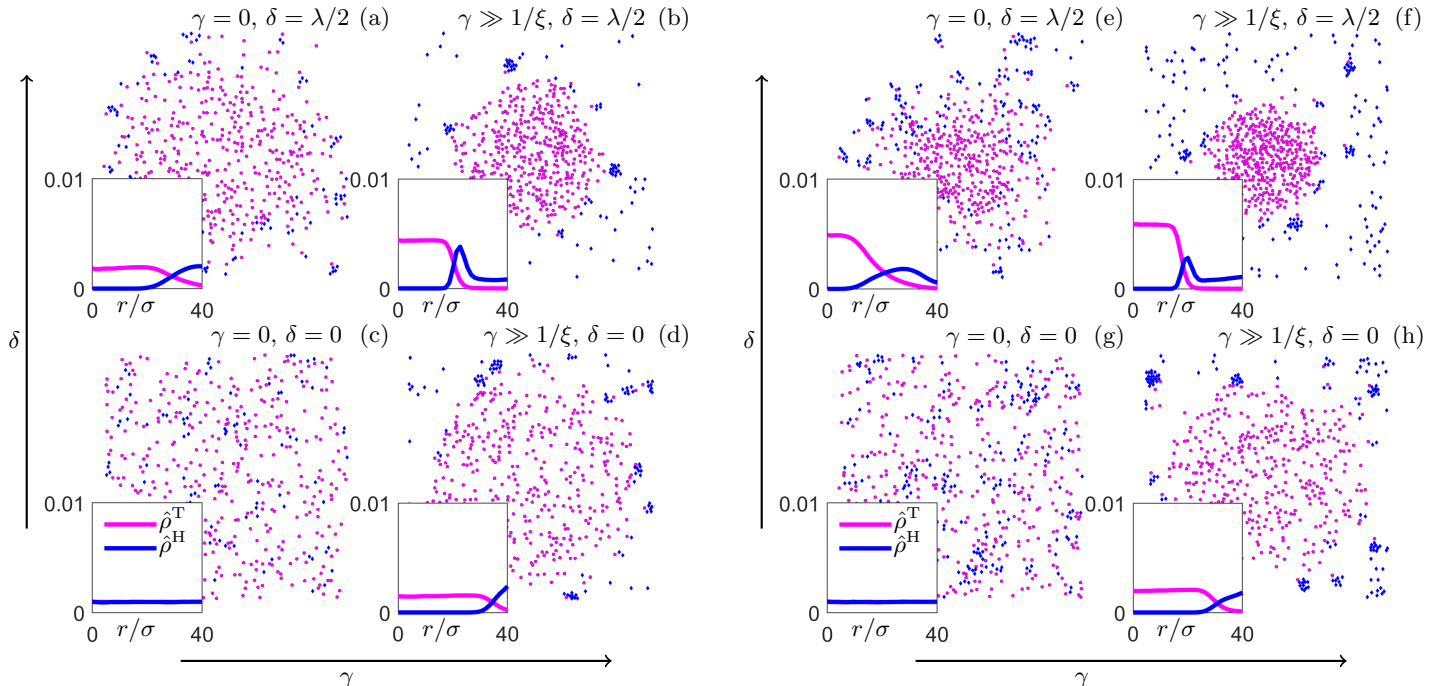


FIG. S1: Snapshots of typical long time configurations for representative values of the control parameters γ and δ for $N_H = 100$ (a-d) and $N_H = 200$ (e-h); in both cases $N_T = 400$ as for the main text. The insets show the time-averaged and angle-averaged densities of agents, $\hat{\rho}^T(r)$ and $\hat{\rho}^H(r)$, as a function of the distance r from the origin for $r \leq L/2$. The simulations show no significant difference with respect to those presented in the main text.

D. Impact of the geometry of the goal region

The agent-based results in Fig. 3 of the main text are based on the assumption of a circular goal region centered around the origin, consistent with the established shepherding literature [1, 4]. Importantly, this circular geometry influences both steps of the decision-making process of the herders, namely (i), the selection rule for \mathbf{T}_i^* [Eq. (1) of the main text] that is based on the distance of targets from the origin, and (ii), the specification of the herder's positioning relative to \mathbf{T}_i^* that is crucial for the trajectory planning.

To explore the possible role of geometry on the shepherding dynamics we here present, as an alternative, agent-based results for a rectangular geometry. Concretely, the simulations are still performed in two dimensions (in a square box of side length L with periodic boundary conditions), but the goal region is now defined as a stripe centered around the origin at $x = y = 0$ and extending along the y -direction. To realize this goal, each herder i now selects its target \mathbf{T}_i^* based on the maximum distance of each target a from the y -axis, that is, based on the x -component $\mathbf{T}_{a,x}$. The selection rule then becomes

$$\mathbf{T}_i^* = \frac{\sum_{a \in N_{i,\xi}} e^{\gamma(|\mathbf{T}_{a,x}| - |\mathbf{H}_{i,x}|)} \mathbf{T}_a}{\sum_{a \in N_{i,\xi}} e^{\gamma(|\mathbf{T}_{a,x}| - |\mathbf{H}_{i,x}|)}}. \quad (\text{S1})$$

Furthermore, herders position themselves behind \mathbf{T}_i^* with shift vector $\hat{\mathbf{T}}_i^* = \text{sign}(\mathbf{T}_{i,x}^*) \hat{\mathbf{x}}$, where $\hat{\mathbf{x}}$ is the unit vector in x -direction. Accordingly, the control input \mathbf{u}_i for each herder becomes

$$\mathbf{u}_i = -(\mathbf{H}_i - (\mathbf{T}_i^* + \delta \text{sign}(\mathbf{T}_{i,x}^*) \hat{\mathbf{x}})) \quad (\text{S2})$$

The remaining dynamical elements from Eq. (7-8) in the Methods and discussed in the main text are preserved. Figure S2 presents snapshots of the agent-based simulations for different values of control parameters γ and δ , along with the corresponding agent densities along the x direction, $\hat{\rho}^T(x)$ and $\hat{\rho}^H(x)$. The numerical density calculations follow a methodology similar to that used for the radial densities $\hat{\rho}^T(r)$ and $\hat{\rho}^H(r)$ in the circular case, with two key differences: first, we compute histograms using Cartesian coordinates (x, y) rather than polar coordinates (r, θ) , and second, we integrate over the y axis instead of averaging over the polar angle θ . Additionally, unlike the radial case

where geometric constraints limited our analysis to agents within a circle of radius $L/2$, here we include all agents in our density calculations. The density profiles exhibit striking similarities between the circular and rectangular geometries. Notably, the rectangular configuration's snapshots demonstrate that the system can be effectively reduced to a one-dimensional setting through y -axis averaging. This simplification establishes direct connections to our one-dimensional continuum framework and supports our assertion that one-dimensional field theories can capture the essential features of the shepherding problem.

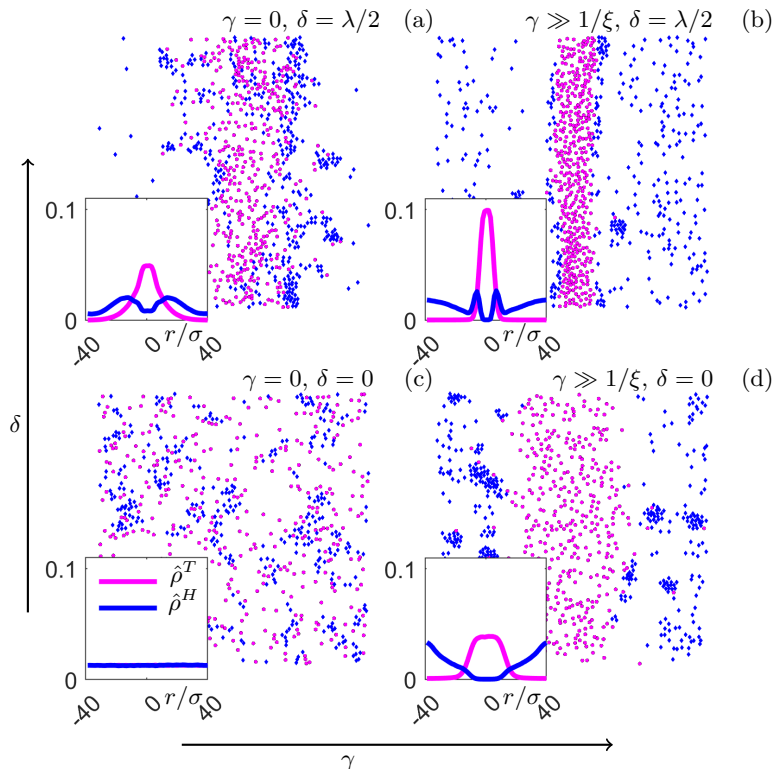


FIG. S2: Long-time configurations of the agent-based system for exemplary values of the two control parameters γ and δ ; the insets represent the time-averaged histograms of targets $\hat{\rho}^T(x)$ and herders $\hat{\rho}^H(x)$ as a function of the relative position from the y -axis x , obtained from the 2 dimensional histogram after integrating over the y direction. At $\gamma = \delta = 0$ we observe a disordered state with homogeneous density distribution (c). The other panels show that, as soon as δ or γ are non zero, inhomogeneous configurations are reached (consistent with Eq. (6) of the main text), where we observe that herders tend to surround targets.

E. Robustness of results for the fraction of confined targets

A key order parameter to characterize the inhomogeneous steady state resulting from the shepherding process is the fraction of confined targets, $\chi(R)$, within a circle of radius R centered around the origin, see Fig. 4(a) of the main text. In these agent-based calculations, R has been chosen based on the fitted density profile of the targets in the case with the largest considered values for both γ and δ . Here we present data for two alternative choices of R . These are inspired by the fact that the targets in our model are represented by mutually repelling disks. It is well known that hard-disk systems, in thermal equilibrium, exhibit a first-order freezing transition from a fluid into a solid state [12]. Considering the target distribution within the goal region as solid-like, we can deduce the radii related to the minimum and maximum area fraction in such a solid, yielding $R^{\min} \sim \sqrt{N_T \sigma^2 / (1.15\pi)}$ and $R^{\max} \sim \sqrt{N_T \sigma^2 / (0.9\pi)}$. The resulting phase diagrams (obtained after time- and ensemble averaging in the steady state) are shown in Fig. S3(a-b). Comparing with the original result we conclude that the precise choice of R has no significant impact on the structure of the diagram.

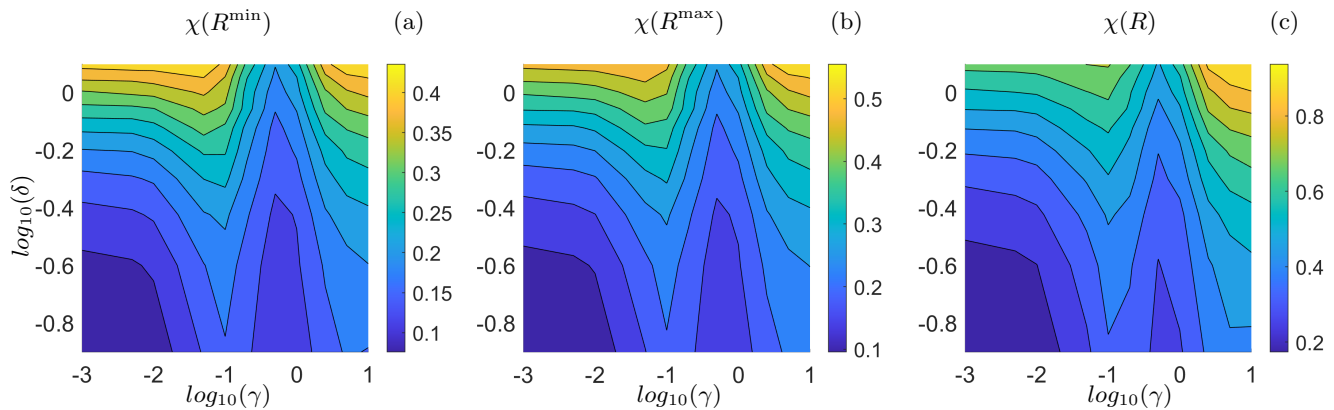


FIG. S3: Fraction of confined targets $\chi(R)$ for different choices of the size of the goal region, R , in the steady state of the agent-based simulations. (a-b) The values of R are derived from the minimum and maximum allowed densities for a solid phase of hard spheres in 2D [12]. These two values are $R^{\min} \sim \sqrt{N_T \sigma^2 / (1.15\pi)}$ and $R^{\max} \sim \sqrt{N_T \sigma^2 / (0.9\pi)}$. (c) Results for the value of R considered in the main text, which are the same of those shown in Fig. 4(a) of the main text. We can see that there is no significant difference in the behaviour of $\chi(\gamma, \delta)$.

II. CONTINUUM THEORY

A. Derivation of coupling functions

In this section we provide details on the derivation of the one-dimensional field equations (3-4) of the main text for the targets and herder densities, $\rho^T(x, t)$ and $\rho^H(x, t)$, respectively (see the Methods for a summary). The field equations for these conserved fields take the general form [9]

$$\partial_t \rho(x, t) = -\nabla [\langle F \rangle(x, t) \rho(x, t)] + D \nabla^2 \rho(x, t) \quad (\text{S3})$$

where the average force $\langle F \rangle(x, t)$ at position x and time t is derived from the microscopic forces $F_{i(a)}$ acting on individual agents through a mean-field assumption. Specifically, we employ the following "recipe":

$$F_i(t) = \sum_{j \in \mathcal{N}_i} F_{ji}(t) \rightarrow \langle F(x, t) \rangle = \int_{\mathbb{B}(x)} F(x, y) \rho(y, t) dy \quad (\text{S4})$$

where $\mathbb{B}(x)$ denotes the finite interaction range between the agents centered around x . As explained in the Methods, the function $F(x, y)$ is translationally invariant (i.e., $F(x, y) = F(x - y)$) for the short-range and long-range repulsion in Eqs. (7-8) while it is not for the "force" imposed by the feedback control input in the dynamics of the herders. In any case, direct computation of the integral over y is not possible since the density $\rho(y, t)$ is not known a priori. Following standard procedures [9], we employ in all cases a gradient expansion

$$\rho(y) \simeq \rho(x) + \nabla \rho(x)(y - x) + \mathcal{O}(\nabla^2 \rho(x)) \quad (\text{S5})$$

where we take into account (at most) the term linear in the gradient.

We first apply the recipe of Eq. (S4) with Eq. (S5) to the pairwise repulsive forces $\mathbf{F}_{\text{SR(LR)}}^{\text{rep}}$ that share the same functional form [see Eq (9)] and, crucially, depend only on agents relative distances. Therefore, the corresponding kernels satisfy the condition of translational invariance; $F(x, y) = F(x - y)$. We also note that, for each x , we integrate over a domain in y that is symmetric around x , and that $F(x - y)$ is, in our case, an odd function in this domain. As an important consequence we find that the zeroth-order term in the gradient expansion of Eq. (S5) cancels out. Therefore, the leading non-zero contribution comes from the gradient term, yielding

$$\langle F_{\text{SR(LR)}}^{\text{rep}} \rangle(x) = \int_{x-\sigma}^{x+\sigma} F_{\text{SR(LR)}}^{\text{rep}}(x - y)(y - x) dy \nabla \rho(x) \quad (\text{S6})$$

where we have used that $\nabla \rho(x)$ is independent of y and can therefore be pulled out of the integral.

From Eq. (S6) we obtain for the short-range (SR) average forces

$$k^{\text{rep}} \langle F^{\text{SR}} \rangle (x) = k^{\text{rep}} \int_{x-\sigma}^{x+\sigma} \text{sign}(x-y)(\sigma - |x-y|)(y-x) \nabla \rho(x) dy = -\alpha^{\text{SR}} \nabla \rho(x) = -k^{\text{rep}} \frac{\sigma^3}{3} \nabla \rho(x) \quad (\text{S7})$$

Analogously, the contribution from the LR forces follows as

$$k^{\text{T}} \langle F^{\text{LR}} \rangle (x) = k^{\text{T}} \int_{x-\lambda}^{x+\lambda} F_{\text{LR}}^{\text{rep}}(x-y)(y-x) \nabla \rho(x) dy = -\alpha^{\text{LR}} \nabla \rho(x) = -k^{\text{T}} \frac{\lambda^3}{3} \nabla \rho(x) \quad (\text{S8})$$

We now turn to the feedback control term that represents decision-making. As discussed in the Methods, the corresponding kernel describing how the herders select the target to chase and how to place themselves relative to the target is not translationally invariant (since the decision-making depends on agent positions relative to the goal region at $x = 0$), that is, $F(x, y)$ also depends separately on x and y . To make the calculations feasible we linearize the exponent and neglect the denominator in the selection rule (see Methods), yielding

$$F^{\text{DM}}(x, y) = -k^{\text{H}}(1 + \gamma(|y| - |x|))(x - (y + \text{sign}(y)\delta)). \quad (\text{S9})$$

As a consequence of the lacking translational invariance, the symmetry arguments used above, which lead to the vanishing of the zeroth order term in the gradient expansion, do not apply any more. Thus, the general form of this term is given by

$$\langle F^{\text{DM}} \rangle (x) = \int_{x-\xi}^{x+\xi} F^{\text{DM}}(x, y) (\rho(x) + \nabla \rho(x)(y-x)) dy = g_1(x)\rho(x) + \nabla \rho(x)g_2(x) \quad (\text{S10})$$

where $g_1(x)$ and $g_2(x)$ are functions depending explicitly on x (rather than constants as in the case of translational invariance discussed before). Clearly, $g_{1,2}(x)$ also depend on the parameters γ and δ , but we drop this here for notational ease.

To proceed, we differentiate the domain into three regions: (i) $x \in [-\xi, 0]$ and $x \in [0, \xi]$, (ii) $x \in (\xi, L/2 - \xi]$ and $x \in (-L/2 + \xi, -\xi]$, (iii) $x \in (L/2 - \xi, L/2)$ and $x \in [-L/2, -L/2 + \xi]$. We here focus on the intervals $x \in [0, \xi]$ and $x \in (\xi, L/2 - \xi]$, the other cases follow analogously. Starting with $g_1(x)$, we find for $0 \leq x \leq \xi$

$$\begin{aligned} g_1(x)|_{x \in [0, \xi]} &= -k^{\text{H}} \int_{x-\xi}^{x+\xi} (1 + \gamma(|y| - |x|))(x - (y + \text{sign}(y)\delta)) dy = \\ &= -k^{\text{H}} \left(\int_{x-\xi}^0 (1 + \gamma(-y-x))(x - (y - \delta)) dy + \int_0^{\xi} (1 + \gamma(y-x))(x - (y + \delta)) dy \right) = \\ &= k^{\text{H}} \delta (1 - 2\gamma x)(x - \xi) + \delta(x + \xi) + \gamma x(\xi^2 - x^2) + \frac{2}{3}\gamma x^3 \end{aligned} \quad (\text{S11})$$

For the interval $\xi < x < L/2 - \xi$, the calculations are simpler since y keeps the same sign throughout the integration domain. We obtain:

$$\begin{aligned} g_1(x)|_{x \in (\xi, L/2 - \xi]} &= -k^{\text{H}} \int_{x-\xi}^{x+\xi} (1 + \gamma(|y| - |x|))(x - (y + \text{sign}(y)\delta)) dy = \\ &= -k^{\text{H}} \int_{x-\xi}^{x+\xi} (1 + \gamma(y-x))(x - (y + \delta)) dy = \\ &= 2\delta\xi + \frac{2}{3}\gamma\xi^3 \end{aligned} \quad (\text{S12})$$

Similar calculations can be performed for $g_2(x)$. Starting with the interval $0 \leq x \leq \xi$, we find

$$\begin{aligned} g_2(x)|_{x \in [0, \xi]} &= -k^{\text{H}} \int_{x-\xi}^{x+\xi} (1 + \gamma(|y| - |x|))(x - (y + \text{sign}(y)\delta))(y-x) dy = \\ &= -k^{\text{H}} \left(\int_{x-\xi}^0 (1 + \gamma(-y-x))(x - (y - \delta))(y-x) dy + \int_0^{\xi} (1 + \gamma(y-x))(x - (y + \delta))(y-x) dy \right) = \\ &= k^{\text{H}} \delta (1 - \gamma x)(\xi^2 - x^2) + \frac{\delta\gamma + 1}{3} 2\xi^3 - \frac{2\gamma x}{3}(\xi^3 - x^3) + \frac{\gamma}{2}(x^4 - \xi^4) \end{aligned} \quad (\text{S13})$$

whereas for $\xi < x < L/2 - \xi$,

$$\begin{aligned} g_2(x)|_{x \in (\xi, L/2 - \xi]} &= -k^H \int_{x-\xi}^{x+\xi} (1 + \gamma(|y| - |x|))(x - (y + \text{sign}(y)\delta))(y - x) dy = \\ &= -k^H \int_{x-\xi}^{x+\xi} (1 + \gamma(y - x))(x - (y + \delta))(y - x) dy = \\ &= k^H \frac{2}{3} (\gamma\delta + 1) \xi^3 \end{aligned} \quad (\text{S14})$$

Using the same steps for the other intervals we finally obtain the expressions of $g_1(x)$ and $g_2(x)$ reported in Eqs. (15-16) in the Methods. As explained there, the functions $g_1(x)$ and $g_2(x)$ coincide with the functions $v_1(x)$ and $v_2(x)$ in Eq. (3-4) of the main text up to a constant factor derived from the adimensionalization of the equations.

1. Higher order terms in the gradient expansion

In this section we briefly consider consequences of including higher order terms in the gradient expansion given in Eq. (S5). The field equations describing the dynamics of $\rho^H(x, t)$ and of $\rho^T(x, t)$ will then have the form

$$\partial_t \rho^T = \nabla \cdot \left[D^T(\rho^T) \nabla \rho^T + \tilde{k}^T \rho^T \nabla \rho^H + \rho^T \sum_{i=3}^Z w_i \nabla^{(i-1)} \rho^H \right] \quad (\text{S15})$$

$$\partial_t \rho^H = \nabla \cdot \left[D^H(\rho^H) \nabla \rho^H - v_1(x) \rho^H \rho^T - v_2(x) \rho^H \nabla \rho^T + \rho^H \sum_{i=3}^Z v_i(x) \nabla^{(i-1)} \rho^T \right] \quad (\text{S16})$$

where Z is maximum order of the expansion we consider, and w_i and $v_i(x)$ are the corresponding couplings. Notice that, as argued before, the coupling functions w_i have to be constant since all kernels related to the interactions in the target's dynamics are translationally invariant. On the other hand, the decision-making interaction kernel in the herders' dynamics is not translationally invariant; this yields the x -dependence of $v_i(x)$.

As shown in the main text, for the continuum equation system up to linear order in the gradients, there is no homogeneous steady state. Interestingly, this statement holds for *any* order Z of the gradient expansion. To see this, we evaluate Eqs. (S15) and (S16) at $\rho^H = \rho_0^H$, $\rho^T = \rho_0^T$, yielding

$$\rho_0^T \sum_{i=3}^Z w_i \nabla^{(i-1)} \rho_0^H = 0 \quad (\text{S17})$$

$$\rho_0^H \sum_{i=3}^Z v_i(x) \nabla^{(i-1)} \rho_0^T = 0, \quad \forall Z \geq 3 \quad (\text{S18})$$

The above relations imply that Eq. (6) of the main text holds true at any order Z of the gradient expansion. We conclude that the "shepherding" inhomogeneities that we observe are *not* just a by-product of the order of truncation of the gradient expansion of Eq. S5; rather they result from the decision-making itself.

B. Analysis in the absence of decision-making

Without decision-making (i.e., $\gamma = 0$, $\delta = 0$), the interaction kernel Eq. (S9) becomes translationally invariant, that is,

$$F^{\text{DM}}(x, y)|_{\gamma=0, \delta=0} = -k^H(x - y). \quad (\text{S19})$$

As a result, the functions $g_1(x)$ and $g_2(x)$ appearing in Eq. (S10) reduce to constants, and we recover expressions similar to those found for the repulsive interaction kernel. Specifically,

$$\begin{aligned} g_1(x) &= 0 \\ g_2(x) &= \frac{2}{3} k^H \xi^3 = g_2^0 \end{aligned} \quad (\text{S20})$$

The resulting equations can be written as

$$\partial_t \rho^T = \nabla \cdot \left[D^T(\rho^T) \nabla \rho^T + \tilde{k}^T \rho^T \nabla \rho^H \right] \quad (\text{S21})$$

$$\partial_t \rho^H = \nabla \cdot \left[D^H(\rho^H) \nabla \rho^H - v_2^0 \rho^H \nabla \rho^T \right] \quad (\text{S22})$$

where the density-dependent couplings $D^T(\rho^T)$ (with A=H,T) and the constants \tilde{k}^T and v_2^0 are defined in the Methods. The above equations involve nonreciprocal cross-diffusive couplings $\nabla \cdot [\rho^A \nabla \rho^B]$ akin of the nonreciprocal Cahn-Hilliard model [9, 13]. The new coupling $\nabla \cdot [v_1(x) \rho^T \rho^H]$ arising from herders' decision-making is absent, as expected at $\gamma = \delta = 0$.

We now perform a linear stability analysis (LSA) around the homogeneous, stationary state $\rho^H(x, t) = \rho_0^H$ and $\rho^T(x, t) = \rho_0^T$ which corresponds to the trivial solution of Eqs. (S21) and (S22). To this end we introduce small fluctuations, i.e.,

$$\rho^A(x, t) = \rho^0 + \delta \rho^A(x, t) \quad (\text{S23})$$

and linearize the field equations in these fluctuations, yielding

$$\partial_t \delta \rho^T(x, t) = D^T(\rho_0^T) \nabla^2 \delta \rho^T(x, t) + \rho_0^T \tilde{k}^T \nabla^2 \delta \rho^H(x, t) \quad (\text{S24})$$

$$\partial_t \delta \rho^H(x, t) = D^H(\rho_0^H) \nabla^2 \delta \rho^H(x, t) - v_2^0 \rho_0^H \nabla^2 \delta \rho^T(x, t) \quad (\text{S25})$$

We expand the fluctuations in a Fourier series, assuming that the growth rate $\Omega(q)$ is the same for both fields, that is

$$\delta \rho^A(x, t) = \int dq e^{iqx + \Omega(q)t} \hat{\rho}^A(q) \quad (\text{S26})$$

Stability of the homogeneous, stationary state implies that the real part of the growth rate $\Omega(q)$, $\text{Re}(\Omega)$, is negative for all nonzero wavenumbers q (note that fluctuations at $q = 0$ cannot occur anyway due to particle number conservation). Inserting the ansatz (S26) into the linearized field equations (S25), (S24) we obtain the eigenvalue problem

$$-q^2 \begin{bmatrix} D^T(\rho_0^T) & \tilde{k}^T \rho_0^T \\ -v_2^0 \rho_0^H & D^H(\rho_0^H) \end{bmatrix} \mathbf{v}(q) = \Omega(q) \mathbf{v}(q) \quad (\text{S27})$$

where the eigenvalues $\Omega(q)$ corresponding to the eigenvectors $\mathbf{v}(q)$ are given by

$$\Omega(q) = -q^2 \frac{1}{2} \left(\Omega_0 \pm \sqrt{\Delta} \right) \quad (\text{S28})$$

with

$$\begin{aligned} \Omega_0 &= D^T(\rho_0^T) + D^H(\rho_0^T) \\ \Delta &= (D^T(\rho_0^T) - D^H(\rho_0^T))^2 - 4v_2^0 \tilde{k}^T \rho_0^T \rho_0^H \end{aligned} \quad (\text{S29})$$

For parameter choices corresponding to our microscopic model, where all short-range interactions as well as the long-range herder-target interaction are repulsive, we have $D^A(\rho_0^A) > 0$ (for A = H,T) and $\tilde{k}^T > 0$. Further, $v_2^0 > 0$ which, together with the negative sign of the corresponding term in Eq. (S22), reflects the attraction of herders to the center-of-mass target.

We first consider the case of equal number densities, $\rho_0^H = \rho_0^T$, considered in the main text. In this case, we have $\Delta < 0$ (for $v_2^0 > 0$, $\tilde{k}^T > 0$) such that the eigenvalues become imaginary. However, since $\Omega_0 > 0$, $\text{Re}(\Omega)$ is negative. Thus, the homogeneous steady state is stable. This result of the LSA conforms with the outcome of our numerical simulations as shown in Fig. 3(c) of the main text. Only by incorporating decision-making (that is, by introducing a coupling of the form $\nabla \cdot [v_1(x) \rho^T \rho^H]$ with $\gamma \neq 0$, $\delta \neq 0$) we achieve an inhomogeneous steady state characteristic of shepherding.

Similar considerations apply when we vary the densities ρ_0^T , ρ_0^H (keeping the total mass constant), or when we vary the constants v_2^0 and \tilde{k}^T (keeping them positive). In all of these cases, we find $\text{Re}(\Omega) < 0$. An overview of the results obtained by numerical solution of Eq. (S28) is given in Fig. S4.

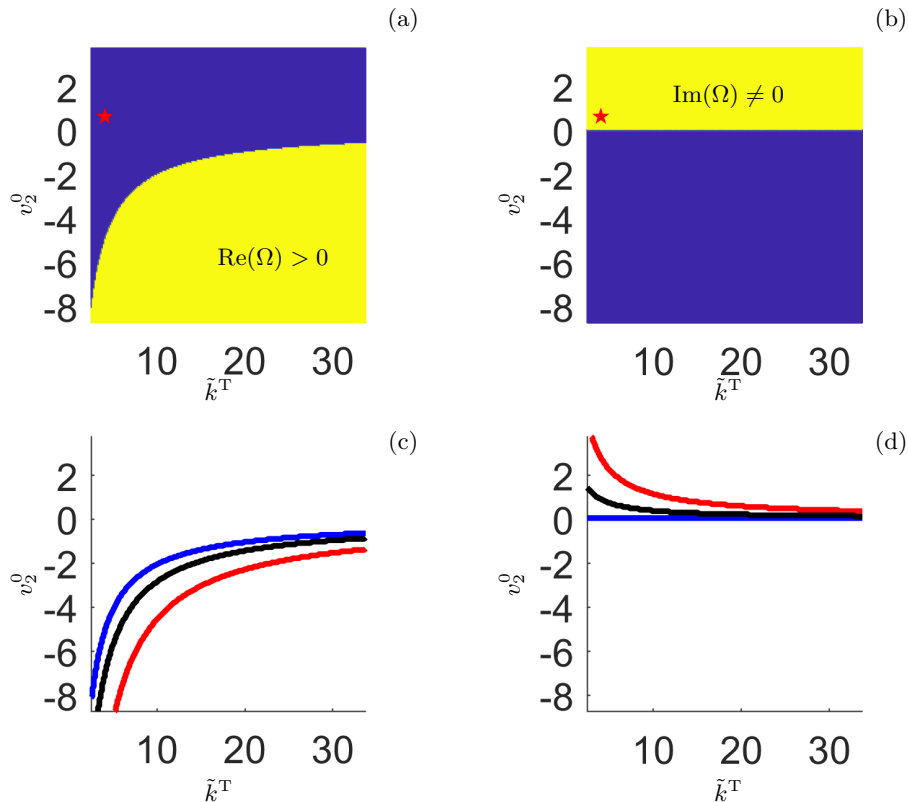


FIG. S4: Results of the LSA around the homogeneous, steady state ($\rho^T(x) = \rho_0^T$, $\rho^H(x) = \rho_0^H$) in the absence of decision-making (i.e., $\gamma = 0$, $\delta = 0$) in the parameter plane spanned by \tilde{k}^T and v_2^0 . Parts (a) and (b) refer to the case $\rho_0^T = \rho_0^H = 0.5\rho_0$ (with $\rho_0 = 0.5/\sigma$) considered in the main text, with the red star indicating the corresponding parameter combination (\tilde{k}^T, v_2^0). Yellow regimes indicate where the real part of one of the growth rates is positive (a) or the imaginary part is nonzero (b). It is seen that the two regimes do not overlap. Parts (c) and (d) refer to the case of different densities (with the total density being the same as before). Here we show the curves dividing regimes with $\text{Re}(\Omega) > 0$ from $\text{Re}(\Omega) \leq 0$ (c) and $\text{Im}(\Omega) \neq 0$ from $\text{Im}(\Omega) = 0$ (d) for three cases: $\rho_0^T = 0.1\rho_0$ (red), $\rho_0^T = 0.5\rho_0$ (blue), and $\rho_0^T = 0.8\rho_0$ (black), with $\rho_0^H = \rho_0 - \rho_0^T$. In all cases, the real part is negative as long as $v_2^0 > 0$, which coincides with the condition for a nonzero imaginary part.

Still, it is interesting to investigate whether and at which coupling parameters the real part of the growth rate can become positive at all. Inspection of Eq. (S28) shows that this can only occur if Δ is positive and its square root exceeds the (positive) term Ω_0 . A necessary requirement is that either $\tilde{k}^T < 0$ (i.e, targets are attracted by herders) or $v_2^0 < 0$ (i.e, herders are repelled by targets), in contradiction to what we have assumed so far. The corresponding parameter regions are indicated in Fig. S4.

Finally, regarding the imaginary part of the growth rate, $\text{Im}(\Omega)$, we see from Fig. S4 that there are no regions where both, $\text{Re}(\Omega) > 0$ and $\text{Im}(\Omega) \neq 0$, since the respective conditions contradict each other. Therefore, for the system without decision-making considered here, we do not find traveling patterns that have been observed in nonreciprocal field theories of phase separating systems [9, 13]. We will later show (see Sec. III of the SI) that traveling patterns can indeed occur for appropriate choices of the decision-making coupling term.

C. Sharpness of the herder-target interface

As shown in Fig. 4(d) of the main text, our continuum theory in presence of decision-making predicts the maximum sharpness of the target-herder interface, σ/Δ , at large values of γ and small values of δ . In contrast, at the agent-based level the maximum is found at large values of both, γ and δ . To explain this difference between the two levels of description we here present an argument based on the functions $v_1(x)$ and $v_2(x)$ entering the field equations Eqs. (3-4) of the main text in presence of decision-making. As we will see, these coupling functions have, to some extent,

competing roles.

To this end, we consider the following simplified scenario. We assume that the targets have already arranged in a confined situation, that is, $\rho^T(x)$ can be described by a hyperbolic-tangent profile, compatible with what is observed at long times in Fig. 2(d). Assuming this profile to be static (i.e., $\partial_t \rho^T = 0$) we can focus on the dynamics of herders alone (once this is understood, we can infer the consequences for the sharpness of the interface).

As a further simplification of the herder dynamics, we approximate the function $v_1(x)$ by $\tilde{v}_1 \text{sign}(x)$ and $v_2(x) = \tilde{v}_2$, as motivated by the actual shape of these functions shown in Fig. S5(a). The definition of the (positive) amplitudes \tilde{v}_1 and \tilde{v}_2 is also indicated in Fig. S5(a). Neglecting short-ranged contributions (contained in $D^H(\rho^H)$), the herder profile then evolves according to

$$\partial_t \rho^H = \nabla \cdot [D \nabla \rho^H - \tilde{v}_1 \text{sign}(x) \rho^H \rho^T - \tilde{v}_2 \rho^H \nabla \rho^T] \quad (\text{S30})$$

Focusing on the region $x \geq 0$, we find from Eq. (S30) that the term involving \tilde{v}_1 drives the herders "to the right" (i.e., larger values of x), whereas the term involving \tilde{v}_2 drives the herders towards higher values of $\rho^T(x)$, which means to move to the "left". In this sense, the two terms have conflicting roles.

If the term $\propto \tilde{v}_1$ dominates (i.e., $\tilde{v}_2 = 0$, or $\tilde{v}_1 \gg \tilde{v}_2$), the herders will all move to the right-most region and push the targets to the left. This will support the system in developing a sharp herder-target interface. However, if we increase \tilde{v}_2 from small values, the herders have to find a balance between the need to move right according to \tilde{v}_1 , and to move left according to \tilde{v}_2 . In this case, the herders will distribute themselves around the interface. Therefore, and since the herders exert a long-range repulsion on the targets, the interface will spread out, causing a decrease of the sharpness.

The preferred localization of herders depending on \tilde{v}_1 and \tilde{v}_2 can be seen more explicitly when we solve the one-dimensional Fokker-Planck Eq. (S30), yielding the steady-state solution [[14]]

$$\begin{aligned} \rho^H(x) &\sim \exp[-V(x)/D] \\ &\equiv \exp \left[\left(\tilde{v}_2 \rho^T(x) + \tilde{v}_1 \int_0^x \rho^T(x') dx' \right) / D \right] \end{aligned} \quad (\text{S31})$$

where $V(x)$ may be interpreted as an effective potential. The minima of $V(x)$ indicate where the herders tend to accumulate. In Fig. S5(c-d) we show that, by increasing \tilde{v}_2 relative to \tilde{v}_1 , the minimum of $V(x)$ moves towards positions with higher values of $\rho^T(x)$. Specifically, the minimum then occurs at the reflection point of the target profile, i.e., the center of the interface. Herders accumulating around this minimum disturb the distribution of targets (through herder-target repulsion), which effectively leads to a "spreading" of the target-herder interface. We conclude that the ratio \tilde{v}_1/\tilde{v}_2 should be a good indicator of the sharpness, σ/Δ .

To close the argument we need to investigate how \tilde{v}_1/\tilde{v}_2 depends on γ and δ . The results are shown in Fig. S5(b). It is seen that the largest values of \tilde{v}_1/\tilde{v}_2 indeed are reached for large γ and small δ values. This is completely consistent with the corresponding dependencies of σ/Δ shown in Fig. 4(d) of the main text.

III. PATTERN DESIGN BEYOND SIMPLE CONTAINMENT

In the main text we discussed how our continuum framework, beyond describing the specific shepherding task illustrated in Fig. 1 of the main text could also be used to model pattern formation in more general decision-making systems (see Fig. 5 of the main text). To this end we propose to vary the spatial profile of the function $v_1(x)$ that multiplies the product of ρ^T and ρ^H in Eq. (3) of the main text. In other words, we consider this function as an *adjustable* control input whose shape can be varied to generate a desired pattern. Below we first discuss the explicit choices for $v_1(x)$ underlying the continuum results in Fig. 5 of the main text. Second, we describe strategies to translate these continuum rules to the agent-based level of description, yielding the microscopic results in Fig. 5 of the main text.

A. Continuum: choices for $v_1(x)$

In all of the four cases considered in Fig. 5 of the main text, the function $v_1(x)$ is a square wave with different periods or phase shifts, while $v_2(x)$ is set to a positive constant, i.e., $v_2(x) = \tilde{v}_2 > 0$. With these choices, the herder dynamics is given by

$$\partial_t \rho^H = \nabla \cdot [D^H(\rho^H) \nabla \rho^H - v_1(x) \rho^H \rho^T - \tilde{v}_2 \rho^H \nabla \rho^T] \quad (\text{S32})$$

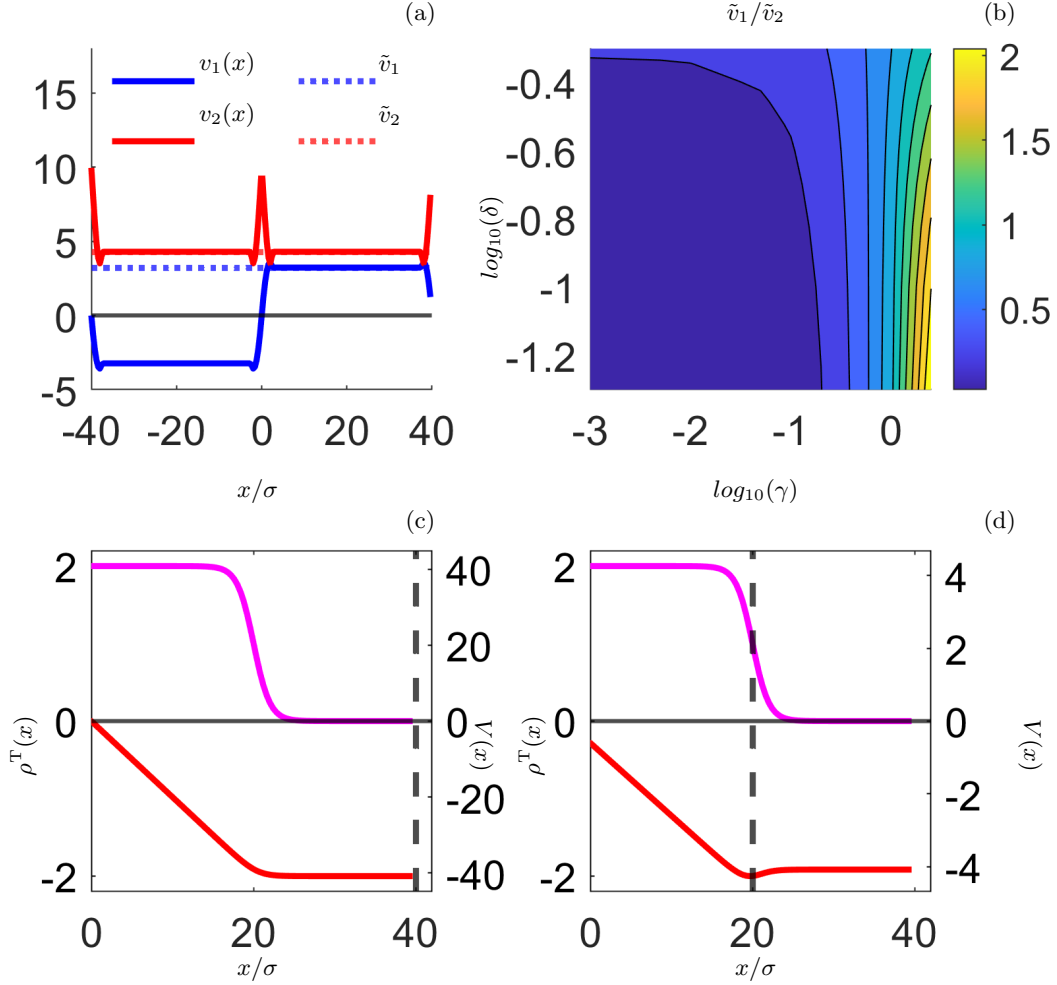


FIG. S5: (a) The functions $v_1(x; \gamma, \delta)$ and $v_2(x; \gamma, \delta)$ defined in the Methods, and their approximated amplitudes $\tilde{v}_1(\gamma, \delta)$ and $\tilde{v}_2(\gamma, \delta)$; the dependence on γ and δ was omitted in the legend for the sake of visibility. (b) The ratio of the amplitudes of v_1 and v_2 , \tilde{v}_1/\tilde{v}_2 as a function of the control parameters γ and δ . As explained in Sec. II C, \tilde{v}_1/\tilde{v}_2 determines the steepness σ/Δ [Fig. 4(d) of the main text]. (c-d) Representative hyperbolic-tangent profile of $\rho^T(x)$ (magenta line) and respective effective potential $V(x)$ (red line) as defined in Eq. (S31) for (c) $\tilde{v}_1 = 0.1$ and $\tilde{v}_2 = 0$, and (d) $\tilde{v}_1 = 0.1, \tilde{v}_2 = 0.2$. Dashed black lines indicate the position of the minimum of $V(x)$. Increasing \tilde{v}_2 , the position of the minimum of $V(x)$ moves towards regions where ρ^T assumes a larger value.

The target dynamics remains unchanged, its evolution equation is given by (see Eq. (4) in the main text)

$$\partial_t \rho^T = \nabla \cdot \left[D^T(\rho^T) \nabla \rho^T + \tilde{k}^T \rho^T \nabla \rho^H \right]. \quad (\text{S33})$$

The concrete choices for $v_1(x)$ in Eq. (S32) corresponding to the four cases in Fig. 5 (main text) are as follows:

- **Containment**

This case corresponds to the herding task discussed in the main part: herders need to collect the targets in a goal region around $x = 0$. In the present study we have *derived* $v_1(x)$ from our agent-based model, yielding the expressions given in Eq. (15) of the Methods. As a simplified ansatz, we can use

$$v_1(x) = \tilde{v}_1 \text{sign}(x) = \tilde{v}_1 \text{sign} \left(\sin \left(\frac{2\pi x}{L} \right) \right) \quad (\text{S34})$$

Here, the appearance of the sin-function in the argument could be replaced by a simpler function that is uneven in x ; e.g., just by x itself. The ansatz (S34) is particularly suitable for comparison with the case of static

patterns discussed below. Irrespective of this detail, Eq. (S34) generates currents of ρ^H to the "right" (to the "left") if a non-zero $\rho^T(x)$ is observed for $x > 0$ ($x < 0$), eventually generating an accumulation of the herders around $x = \pm L/2$. The herder-target repulsion then pushes the targets toward the goal region around $x = 0$.

- **Expulsion**

In another application, herders may want to push targets *away* from a predefined (potentially dangerous) region. This can be realized by reversing the rule given in Eq. (S34), such that

$$v_1(x) = -\tilde{v}_1 \text{sign} \left(\sin \left(\frac{2\pi x}{L} \right) \right) \quad (\text{S35})$$

This choice of $v_1(x)$ generates currents of ρ^H to the "right" (to the "left") if a non-zero $\rho^T(x)$ is observed for $x < 0$ ($x > 0$), eventually leading to the accumulation of the herders around $x = 0$. Targets are then expelled towards the boundary.

Notice that, given the periodicity of the domain, containment around x^* is equivalent to the expulsion from $x^* \pm L/2$: indeed the v_1 -functions for containment [Eq. (S34)] and expulsion [Eq. (S35)] are the same but translated by $L/2$. This means that the two tasks are mathematically equivalent on this level of description.

The two cases discussed so far show that a change of sign of the function $v_1(x)$ around the position x^* produces containment of targets around x^* if $(x - x^*)v_1(x) \geq 0$ (for all $x \neq x^*$), or expulsion from the region around x^* if $(x - x^*)v_1(x) \leq 0$ (for all $x \neq x^*$). This suggests that more sophisticated patterns can be generated by including more zeros into $v_1(x)$. An example is given in the third case considered in Fig. 5 (main text):

- **Static patterns**

We consider a system where herders want to collect targets at several regions centered at positions x_j^* in the domain, where j is a positive integer going from 1 to the number of regions where to collect the targets. As a consequence, the targets will be expelled by the other regions of the domain. In a one-dimensional setup, the desired resulting state would be characterized by a stripe pattern. As an example, we choose $x_{1,2}^* = \pm L/3$ and $x_3^* = 0$ as the positions around which the targets shall be accumulated. This can be realized with

$$v_1(x) = -\tilde{v}_1 \text{sign} \left(\sin \left(\frac{6\pi x}{L} \right) \right) \quad (\text{S36})$$

whose zeros $x_{1,2,3}^*$ satisfy the condition $(x - x_j^*)v_1(x) \geq 0$ for x in a neighborhood of x_j^* ($j = 1, 2, 3$).

- **Traveling patterns**

Finally, it is interesting to consider the simplest choice for the function $v_1(x)$, namely

$$v_1(x) = \tilde{v}_1 = \text{const} \quad (\text{S37})$$

Indeed, as shown in Fig. 5 in the main text, a suitable choice for the constant \tilde{v}_1 produces a traveling pattern, where the herders persist to push the targets across the domain. A corresponding linear stability analysis predicting the occurrence of time-dependent motion is given in Sec. III C.

Intuitively, we can understand the travelling patterns as follows: If $\tilde{v}_1 > 0$ (and $v_2^0 > 0$), the herders will move towards the "right" as long as they observe a non-zero $\rho^T(x)$. This will eventually lead to the accumulation of the herders at the "right" of the targets. However, this cannot be a steady state since the coupling $-\tilde{v}_2 \rho^H \nabla \rho^T$ pushes the herders towards the "left" where the targets are concentrated. This, in turn, will push the target even more towards the "left" as they try to escape the herders [due to the coupling $\tilde{k}^T \rho^T \nabla \rho^H$ in the target dynamics, Eq. (S33)]. As a result, we observe traveling waves to the "left".

B. Agent dynamics: decision-making rules

We now show how to "translate" the design rules represented by the different functions $v_1(x)$ discussed in the preceding section towards the microscopic level of description. To this end we properly design the feedback control input \mathbf{u}_i and combine these expressions with the agent-based Langevin equations given in Eqs. (7-8) of the Methods. To design the control input, we use the same general strategy as in the shepherding case considered in the main text. In particular, the herder's decision-making involves two key elements, namely (i) a selection rule for targets (whose sensitivity is tuned by γ) yielding \mathbf{T}_i^* , and (ii) a planning of the trajectory (controlled by δ). The recipes described below are the basis of the agent-based numerical results shown in Fig. 5 of the main text. All other parameters of the simulations are the same as those used for the simulations used to produce in Fig. 3 of the main text.

- **Containment**

This is the same task analyzed in the main text (see Fig. 3) with the difference that we here employ a rectangular geometry for the goal region, different from the geometry used in the main text (see Sec. ID for the discussion on this point). Specifically, we use the following control input for the herders

$$\mathbf{u}_i = -(\mathbf{H}_i - (\mathbf{T}_i^{*,\text{cont}} + \delta \text{sign}(\mathbf{T}_{i,x}^{*,\text{cont}}))) \quad (\text{S38})$$

where

$$\mathbf{T}_i^{*,\text{cont}} = \frac{\sum_{a \in N_{i,\xi}} e^{\gamma(|\mathbf{T}_{a,x}| - |\mathbf{H}_{i,x}|)} \mathbf{T}_a}{\sum_{a \in N_{i,\xi}} e^{\gamma(|\mathbf{T}_{a,x}| - |\mathbf{H}_{i,x}|)}}, \quad (\text{S39})$$

These rules eventually generate an accumulation of the herders around $x = \pm L/2$, pushing the targets into the region around $x = 0$.

- **Expulsion**

As discussed above at the continuum level (see Sec. III A), containment around a given position x^* is equivalent to the expulsion from $x^* \pm L/2$ (which are the points with largest distance from x^*) due to the periodicity of the domain. As a consequence, to generate expulsion from $x = 0$ we design the selection rule so as to select the target with the largest distance from $x^* = L/2$ (which coincides with $x^* = -L/2$). This yields

$$\mathbf{T}_i^{*,\text{exp}}(\gamma) = \frac{\sum_{a \in N_{i,\xi}} e^{\gamma((L/2 - |\mathbf{T}_{a,x}|) - (L/2 - |\mathbf{H}_{i,x}|))} \mathbf{T}_a}{\sum_{a \in N_{i,\xi}} e^{\gamma((L/2 - |\mathbf{T}_{a,x}|) - (L/2 - |\mathbf{H}_{i,x}|))}} = \frac{\sum_{a \in N_{i,\xi}} e^{-\gamma(|\mathbf{T}_{a,x}| - |\mathbf{H}_{i,x}|)} \mathbf{T}_a}{\sum_{a \in N_{i,\xi}} e^{-\gamma(|\mathbf{T}_{a,x}| - |\mathbf{H}_{i,x}|)}} = \mathbf{T}_i^{*,\text{cont}}(-\gamma) \quad (\text{S40})$$

The third and fourth member of these equations show that selection of target the largest distance from $x^* = L/2$ is equivalent to the target selection rule Eq. (S38) we used for containment, yet with negative γ . Indeed, the choice $\gamma < 0$ implies selection of the target with the smallest (rather than the largest) distance from the origin. Regarding the trajectory planning, following the same reasoning, we want the herders to place themselves *between* the selected target and the origin. Therefore, we can again use the same formulation as in the containment case [Eq. (S38)], but now the herders place themselves with a shift $-\delta \text{sign}(\mathbf{T}_{i,x}^*)$. The control input then becomes

$$\mathbf{u}_i = -(\mathbf{H}_i - (\mathbf{T}_i^* - \delta \text{sign} \mathbf{T}_{i,x}^{*,\text{cont}}(-\gamma))) \quad (\text{S41})$$

with $0 < \delta < \lambda$, and $1/\xi \ll \gamma$.

- **Static patterns**

To create a static stripe-like pattern, we follow the strategy described on the continuum level where $v_1(x)$ was chosen as a square wave whose reflection points correspond to the centers of containment regions. In other words, the task of creating a stripe patterns is divided into several containment tasks, each involving one "accumulation point" x^* . This motivates to formulate the selection rule as follows: If one herder, say herder i , observes a target a in its sensing region, it first identifies the accumulation points x^* to which this herder and the target are the closest (among the set of accumulation points). We refer to these two special accumulation points as x_i^* and x_a^* , respectively. The selection rule can then be written as

$$\mathbf{T}_i^* = \frac{\sum_{a \in N_{i,\xi}} e^{\gamma(|\mathbf{T}_{a,x} - x_a^*| - |\mathbf{H}_{i,x} - x_i^*|)} \mathbf{T}_a}{\sum_{a \in N_{i,\xi}} e^{\gamma(|\mathbf{T}_{a,x} - x_a^*| - |\mathbf{H}_{i,x} - x_i^*|)}} \quad (\text{S42})$$

For the trajectory planning, we accordingly require the herder to place itself at the back of the target with respect to x_a^* . We note that x_a^* can vary during the motion of all agents (contrary to the fixed goal regions considered in the other cases). Therefore, we write the control input as

$$\mathbf{u}_i = -(\mathbf{H}_i - \mathbf{H}_i^*(\gamma, \delta)) \quad (\text{S43})$$

where \mathbf{H}_i^* is the desired position for herder i defined as

$$\mathbf{H}_i^*(\gamma, \delta) = \frac{\sum_{a \in N_{i,\xi}} e^{\gamma(|\mathbf{T}_{a,x} - x_a^*| - |\mathbf{H}_{i,x} - x_i^*|)} (\mathbf{T}_a + \delta \text{sign}(\mathbf{T}_{a,x} - x_a))}{\sum_{a \in N_{i,\xi}} e^{\gamma(|\mathbf{T}_{a,x} - x_a^*| - |\mathbf{H}_{i,x} - x_i^*|)}} \quad (\text{S44})$$

Notice that this strategy requires the herders to know the positions of the multiple accumulation points x^* .

• Travelling patterns

As discussed in the continuum part, numerical simulations of the field equations with $v_1(x) = \tilde{v}_1$ (as well as the corresponding linear stability analysis) reveal for suitable choices of the constants \tilde{v}_1 and \tilde{v}_2 a travelling pattern. Specifically, for $\tilde{v}_1 > 0$, the coupling $\tilde{v}_1 \rho^T \rho^H$ generates a persistent travelling wave moving to the "left". On the agent-based level, we can create such a situation with a selection rule that favors the target with the largest value of the x coordinate in the sensing region of herder i

$$\mathbf{T}_i^{*,\text{trav patt}} = \frac{\sum_{a \in N_{i,\xi}} e^{\gamma(\mathbf{T}_{a,x} - \mathbf{H}_{i,x})} \mathbf{T}_a}{\sum_{a \in N_{i,\xi}} e^{\gamma(\mathbf{T}_{a,x} - \mathbf{H}_{i,x})}}, \quad (\text{S45})$$

We combine this rule with the requirement that a herder always places itself to the "right" of the target, in the $x > 0$ direction. This is achieved by writing the distributed control input for herder i as

$$\mathbf{u}_i = -(\mathbf{H}_i - (\mathbf{T}_i^{*,\text{trav patt}} + \delta)) \quad (\text{S46})$$

C. Linear stability analysis for the case of constant coefficients \tilde{v}_1 and \tilde{v}_2

Putting the functions $v_1(x)$ and $v_2(x)$ in the full herder dynamics to constants, we arrive at the coupled PDEs

$$\partial_t \rho^T = \nabla \cdot [D^T(\rho^T) \nabla \rho^T + \tilde{k}^T \rho^T \nabla \rho^H] \quad (\text{S47})$$

$$\partial_t \rho^H = \nabla \cdot [D^H(\rho^H) \nabla \rho^H - \tilde{v}_1 \rho^H \rho^T - \tilde{v}_2 \rho^H \nabla \rho^T] \quad (\text{S48})$$

We first note that a trivial steady state solution for the above equations is given by $\rho^T(x) = \rho_0^T$, $\rho^H(x) = \rho_0^H$, corresponding to a homogeneous steady state. This is in stark contrast to the case of a space-dependent function $v_1(x)$ that does not allow for such a steady state, as discussed in the main text (see Eq. (6)).

We now perform a linear stability analysis (LSA) around the homogeneous solution, following the procedure outlined in Sec. II B (where we considered the system without decision-making). Introducing small fluctuations $\delta \rho^A(x, t)$ with $A = H, T$ [see Eq. (S23)] and linearizing Eqs. (S48) we obtain

$$\partial_t \delta \rho^T(x, t) = D^T(\rho_0^T) \nabla^2 \delta \rho^T(x, t) + \rho_0^T \tilde{k}^T \nabla^2 \delta \rho^H(x, t) \quad (\text{S49})$$

$$\partial_t \delta \rho^H(x, t) = D^H(\rho_0^H) \nabla^2 \delta \rho^H(x, t) - \tilde{v}_2 \rho_0^H \nabla^2 \delta \rho^T(x, t) - \tilde{v}_1 (\rho_0^T \nabla \delta \rho^H(x, t) + \rho_0^H \nabla \delta \rho^T(x, t)) \quad (\text{S50})$$

Next, we expand the fluctuations in a Fourier series [see Eq. (S26)]. Insertion into Eqs. (S50) and (S49) brings us to the eigenvalue problem

$$-q \begin{bmatrix} q D^T(\rho_0^T) & q \tilde{k}^T \rho_0^T \\ -q \tilde{v}_2 \rho_0^H + i \tilde{v}_1 \rho_0^H & q D^H(\rho_0^H) + i \tilde{v}_1 \rho_0^T \end{bmatrix} \mathbf{v}(q) = \Omega(q) \mathbf{v}(q) \quad (\text{S51})$$

where we note the different dependency on the wavenumber q as compared to the uncontrolled case [see Eq. (S27)]. A further difference is that the two matrix elements involving \tilde{v}_1 are complex (due to the product of densities appearing in the related current). As a consequence, if $\tilde{v}_1 \neq 0$, the growth rate $\Omega(q)$ has always an imaginary part.

To decide about the (linear) stability of the homogeneous steady state, we have to consider the real part of the growth rate, $\text{Re}(\Omega)(q)$. We have performed extensive numerical investigations for a range of the parameters \tilde{v}_1 and the strength of herder-target repulsion, \tilde{k}^T . Results for three wavenumbers q and two values of \tilde{v}_2 (one positive, one negative) are presented in Fig. S6. In the yellow regions, $\text{Re}(\Omega)(q) > 0$ which, together with the nonzero imaginary parts, signals a temporal (oscillatory) instability.

We first consider the case $\tilde{v}_2 > 0$ (top row of Fig. S6), where herders are attracted to the targets (as assumed throughout the rest of this paper). The results show that, for sufficiently strong herder-target repulsion \tilde{k}^T (such as the value considered in the main text, indicated by an orange star), an increase of $|\tilde{v}_1|$ from zero can produce a temporal instability. An exception is the special case $\tilde{v}_1 = 0$ where, consistent with our results in S4, no temporal instability occurs. We further observe from Fig. S6(a-c) that the (yellow) regimes indicating positive growth rates shrink with increasing wavenumber (and completely vanish for large enough q). This can be understood from the fact that the instability is driven by \tilde{v}_1 (providing a term linear in q in Eq. (S51) which competes with all of the other terms that provide a q^2 -contribution in Fourier space (which, as discussed in Sec. II B, would otherwise make the homogeneous state stable).

Turning to the case $\tilde{v}_2 < 0$ (where herders are, on average, repelled by targets), the situation is different, as revealed by the diagrams in the bottom row of Fig. S6). Here, it is seen that the system is temporarily unstable even for $\tilde{v}_1 = 0$. This already indicates that for $\tilde{v}_2 < 0$, the instability is driven by the repulsion between targets and herders (modulated by \tilde{k}^T), represented by a term proportional to q^2 in Eq. (S51). Accordingly, the larger q , the larger the region of the parameters where the homogeneous steady state is unstable.

Finally, we recall that travelling patterns are one of the key effects observed in nonreciprocal systems, e.g., in the Cahn-Hilliard equations for phase-separating systems if the nonreciprocity in the couplings between the fields is sufficiently pronounced [9, 13, 15]. Here we obtain such an oscillatory instability even the case that there is no source of phase separation (such as attraction between particles of one species).

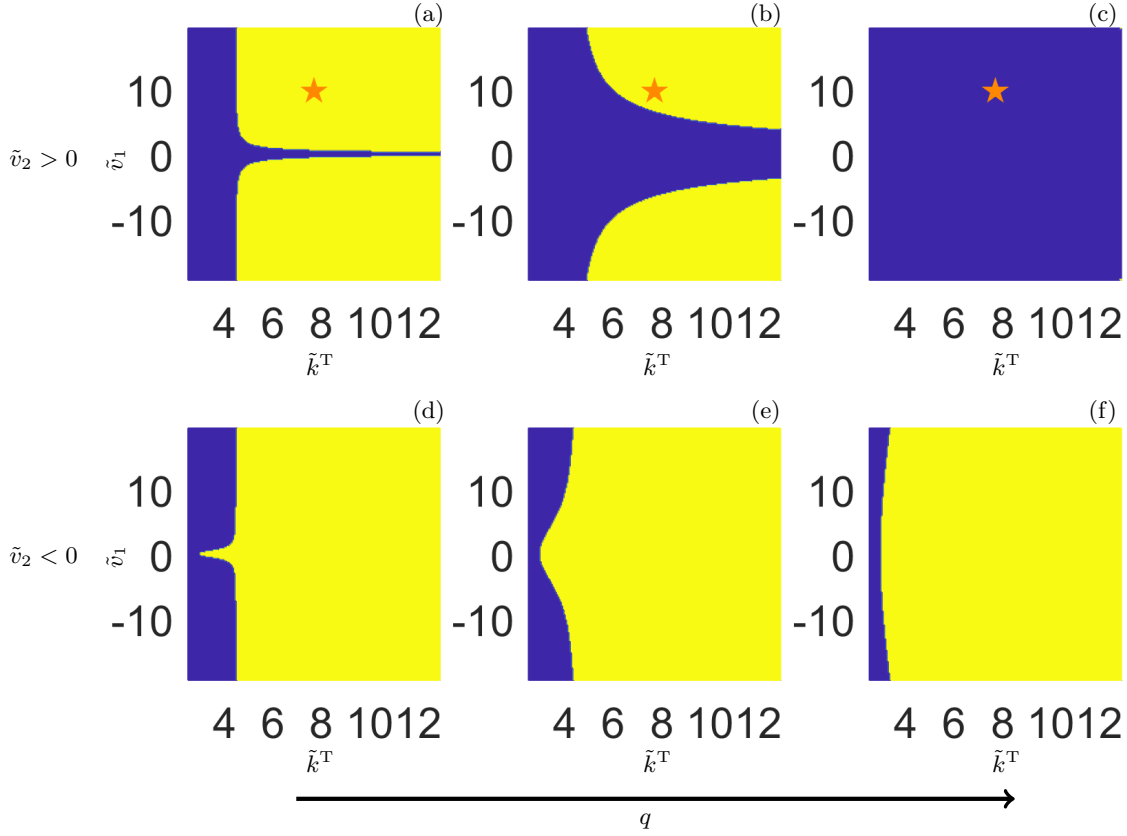


FIG. S6: LSA of the field equations S48 and S47 with respect to a homogeneous steady state. Yellow regions indicate where one of growth rates obtained from Eq. S51 has a positive real part. We present results for both $\tilde{v}_2 > 0$ (a-c) and $\tilde{v}_2 < 0$ (d-f), and for different values of the wavenumber q , increased from left to right with values $q = \frac{2\sigma\pi}{L}[1, 10, 50]$. In all cases, the corresponding imaginary part is non-zero. (a-c) $\tilde{v}_2 > 0$: this is the case discussed in the main text, where herders are attracted to the targets on the field level. The results show that we cannot achieve a positive real part of the growth rates for $\tilde{v}_1 = 0$, consistently with Fig. S4. (d-f) $\tilde{v}_2 < 0$: in this case herders and targets both repel each other. The regions of instability increase with q , differently from the case $\tilde{v}_2 > 0$. The parameter values used in (a-c) are the same as those used in Fig. 5(1) of the main text (see Methods), except for the two varied parameters \tilde{k}^T and \tilde{v}_1 . The precise values related to Fig. 5(1) of the main text correspond to the the orange star. To reproduce panels (d-f), the same values are used, except for k^H whose sign needs to be inverted.

IV. LIST OF SUPPLEMENTARY VIDEOS

1. Supplementary Information Video 1: numerical simulations of the agent-based equations (7-8) of the main text, showing the emergence of containment starting from a homogeneous configuration. The parameters γ and δ are set to the largest considered values, namely $\gamma = 10/\sigma$, $\delta = \lambda/2$. Blue diamonds represent the herders, magenta dots represent the targets.
2. Supplementary Information Video 2: Numerical simulations of the field equations (3-4) of the main text showing the emergence of containment at the continuum level starting from a homogeneous state. The parameters γ and δ are set to the largest considered values, namely $\gamma = 2.5/\sigma$, $\delta = \lambda/2$. The blue and magenta lines respectively represent ρ^H and ρ^T .
3. Supplementary Information Video 3: numerical simulations of the field equations Eq. (S47) and Eq. (S48) showing the emergence of traveling patterns from a perturbed homogeneous state. The numerical values of the parameters are presented in the Methods. The blue and magenta lines represent ρ^H and ρ^T , respectively.
4. Supplementary Information Video 4: agent-based numerical simulations showing the emergence of traveling patterns (see Section III B). Blue diamonds represent the herders, magenta dots represent the targets.

-
- [1] A. Lama and M. di Bernardo, Shepherding and herdability in complex multiagent systems, *Physical Review Research* **6**, L032012 (2024).
 - [2] P. Nalepka, R. W. Kallen, A. Chemero, E. Saltzman, and M. J. Richardson, Herd those sheep: Emergent multiagent coordination and behavioral-mode switching, *Psychological science* **28**, 630 (2017).
 - [3] S. Zhang, X. Lei, M. Duan, X. Peng, and J. Pan, A distributed outmost push approach for multirobot herding, *IEEE Transactions on Robotics* **40**, 1706 (2024).
 - [4] F. Auletta, D. Fiore, M. J. Richardson, and M. di Bernardo, Herding stochastic autonomous agents via local control rules and online target selection strategies, *Autonomous Robots* **46**, 469 (2022).
 - [5] G. Ariel and A. Ayali, Locust collective motion and its modeling, *PLOS computational Biology* **11**, e1004522 (2015).
 - [6] A. Cavagna, A. Culla, X. Feng, I. Giardina, T. S. Grigera, W. Kion-Crosby, S. Melillo, G. Piségnà, L. Postiglione, and P. Villegas, Marginal speed confinement resolves the conflict between correlation and control in collective behaviour, *Nature Communications* **13**, 2315 (2022).
 - [7] G. Sartoretti, M.-O. Hongler, M. E. de Oliveira, and F. Mondada, Decentralized self-selection of swarm trajectories: from dynamical systems theory to robotic implementation, *Swarm Intelligence* **8**, 329 (2014).
 - [8] G. Vásárhelyi, C. Virágh, G. Somorjai, T. Nepusz, A. E. Eiben, and T. Vicsek, Optimized flocking of autonomous drones in confined environments, *Science Robotics* **3**, eaat3536 (2018).
 - [9] Z. You, A. Baskaran, and M. C. Marchetti, Nonreciprocity as a generic route to traveling states, *Proceedings of the National Academy of Sciences* **117**, 19767 (2020).
 - [10] N. Long, K. Sammut, D. Sgarioto, M. Garratt, and H. Abbass, A comprehensive review of shepherding as a bio-inspired swarm-robotics guidance approach], *IEEE Transactions on Emerging Topics in Computational Intelligence* **4**, 523 (2020).
 - [11] S. Van Havermaet, P. Simoens, T. Landgraf, and Y. Khaluf, Steering herds away from dangers in dynamic environments, *Royal Society Open Science* **10**, 230015 (2023).
 - [12] M. Schmidt and H. Löwen, Freezing between two and three dimensions, *Physical review letters* **76**, 4552 (1996).
 - [13] S. Saha, J. Agudo-Canalejo, and R. Golestanian, Scalar active mixtures: The nonreciprocal cahn-hilliard model, *Physical Review X* **10**, 041009 (2020).
 - [14] R. Zwanzig, *Nonequilibrium statistical mechanics* (Oxford university press, 2001).
 - [15] M. Fruchart, R. Hanai, P. B. Littlewood, and V. Vitelli, Non-reciprocal phase transitions, *Nature* **592**, 363 (2021).